npj | materials degradation

Article

Published in partnership with CSCP and USTB

https://doi.org/10.1038/s41529-024-00517-y

The microstructure-corrosion relationships in laser-welded dissimilar steel-to-aluminium joints

J. I. Ahuir-Torres[1], S. Jabar[2] ✉, P. Franciosa[2], D. Ceglarek[2] & H. R. Kotadia[1,2] ✉

This study investigated the corrosion behaviour of dissimilar steel-to-aluminium laser-welded conduction, and keyhole mode (partial- and full-penetration) lap joints through electrochemical techniques and advanced microstructural characterisation. The corrosion resistance of the weld was found to be higher than the base materials, primarily due to the presence of cathodic Fe_xAl_y (η-Fe_2Al_5, θ-Fe_4Al_{13}, β-FeAl) intermetallic compounds (IMCs) with high corrosion potential. The different micro and macro-galvanic corrosion mechanisms were found at various interfaces around the weld, resulting in localised pitting corrosion. The keyhole mode welding showed improved corrosion resistance, primarily attributed to the type, size, and distribution of IMCs.

Steel (Fe) and aluminium (Al) alloys are crucial structural materials widely used in engineering, with steels known for their versatility, offering good creep resistance, formability, and high strength at a low cost. On the other hand, Al alloys provide value in applications requiring light-weighting and corrosion resistance[1,2] Dissimilar joints between steel and Al alloys are vital, particularly in transport industries aiming to reduce overall weight without compromising safety. Nevertheless, challenges have arisen in dissimilar metal welding due to the inherent differences in the properties of the two metallic alloys that require welding together[3]. Physical properties play a direct role in shaping the fusion zone and the subsequent rapid solidification characteristics. Furthermore, solubility and differences in melting temperature have an impact on the weld pool, defects, and the formation of intermetallic compounds (IMCs)[4]. This can have a substantial effect on the properties and structural integrity of the welded joint.

Fusion joining processes involving steel and Al lead to the formation of brittle IMCs, including η-Fe_2Al_5, κ-Fe_3Al, θ-Fe_4Al_{13}, γ-$FeAl_3$, and β-FeAl at the interface and in the weld pool[2,5,6]. In the literature, researchers extensively studied IMCs, their nucleation and growth[2,7], types[4], the influence of different alloying elements[8], and the assessment of mechanical properties[9,10]. IMC formation is influenced by chemical potential, initial interdiffusion nucleation conditions, and constituent element mobilities, which vary based on the welding process and alloy chemistry. Therefore, understanding the dissimilar weld characteristics is essential, as they are strongly correlated with the heat and mass-transfer process within the evolving melt-pools. Then, comprehending the underlying physical mechanisms related to interface formation, dissimilar (liquid) metal mixing, and solidification within the weld pool can facilitate the development of mitigation strategies against the formation of poor-quality dissimilar welded joints[10]. On these topics, recent studies suggest that optimising laser processing parameters can yield a uniform layer of η-Fe_2Al_5 IMCs at the interface between Fe- and Al- rich regions, free from problems like hot and cold cracks, ultimately contributing to improved strengths of up to 4 kN (105.3 N/mm^2)[11].

Furthermore, understanding the corrosion behaviour of dissimilar welds is crucial, particularly given that the joining of two metals can heighten susceptibility to galvanic corrosion (GC) due to micro-segregation and formation of IMCs during dissimilar metal fusion welding, along with the creation of a heat-affected zone (HAZ). Corrosion typically initiates at the welding boundary and manifests as localised attacks around the IMC and precipitation phases at the interface and within the weld[12,13] In general, dissimilar metals, IMCs, and heterogeneity in chemical composition lead to different corrosion potentials when they come into contact with a corrosive environment, GC occurs once certain kinetic conditions are met. However, the precise mechanisms governing the localised initiation and propagation of corrosion at different interfaces of steel to Al laser-welded joints remain incompletely understood. The rapid solidification and thermal cycles during laser welding affect different parts of the joints, leading to significant variations in the microstructure and properties of the resultant joint[4]. Additionally, alterations in laser welding parameters substantially influence weld geometry, IMC types, and distributions[14–16] resulting in varied electrochemical responses in different zones.

Therefore, this research aims to uncover the corrosion mechanisms at different interfaces of dissimilar metal laser welding, including the impact of weld geometry (conduction and keyhole mode) and IMC distribution. The study selected an overlap configuration of IF steel to 1050 Al alloy, achieving three weld shapes by adjusting laser beam welding (LBW) parameters, primarily the core laser power while maintaining a constant laser welding

[1]School of Engineering, Liverpool John Moores University, Liverpool, UK. [2]WMG, University of Warwick, Coventry, UK. ✉e-mail: sharhid.jabar@warwick.ac.uk; h.r.kotadia@ljmu.ac.uk

speed. Electrochemical analysis techniques, including electrochemical noise with asymmetrical system, potentiodynamic polarisation curve, and electrochemical impedance spectroscopy, were applied to test the three welds and a non-welded area in saltwater with varying immersion times for electrochemical impedance spectroscopy. In-depth microstructural analysis before and after the corrosion tests were also performed. The electrochemical and microstructural results confirmed diverse GC mechanisms at different interfaces of dissimilar welds and highlighted the role of weld microstructures from the perspective of pitting corrosion initiation. The outcomes of the study offer valuable insights into the GC of steel (Fe) to Al in the context of the weld.

Results

Pre-corrosion weld microstructure

The weld cross-sections, displayed in Fig. 1 via optical microscopy and SEM, demonstrate the presence of three distinct weld types, encompassing both conduction and keyhole modes (partial and full penetration). Observing the microstructure of these cross-sections, variations in weld geometry are apparent, primarily due to differences in weld penetration depth and width. The classification of welds is based on the aspect ratio, calculated as the ratio of weld depth to weld width. A ratio of ≤1.0 corresponds to the conduction mode, whereas ratios above 1.0 signify the keyhole mode[11]. These differences in weld penetration can be attributed to the varying power levels of the laser, with higher power densities facilitating deeper weld penetration into the Al sheet[11].

Figure 2 illustrates the distinctive (liquid) metal mixing characteristics of each of the three weld pools, leading to the formation of Fe_xAl_y IMCs. Notably, the conduction mode weld (Fig. 2a) exhibits a thin continuous IMC layer at the Al/weld interface, primarily due to limited mixing of the Fe and Al elements. Conversely, in the keyhole modes (both partial and full penetration), the greater fluid-flow lead to a higher degree of mixing (of Fe and Al) which resulted in a different distribution and volume of IMCs within the weld. This phenomenon is clearly evident through the SEM-EDS maps and line scan data displayed in Fig. 2. Based on varying compositions of Fe and Al, different types of Fe_xAl_y IMCs are observed: β-FeAl at 20-30 wt.% Al, η-Fe_2Al_5 at approximately 55 wt.% Al, and θ-Fe_4Al_{13} at Al concentrations exceeding 60 wt.%. Analysis of the line-scan data (Fig. 2e–g) allows for the identification of various IMCs (Fig. 2d) based on changes in elemental concentration. In the conduction mode weld (Fig. 2e), distinct layers of β-FeAl, η-Fe_2Al_5, and θ-Fe_4Al_{13} are discernible. The partial penetration keyhole mode η-Fe_2Al_5 IMC layer was low or absent and the θ-Fe_4Al_{13} IMC was found well distributed throughout the welds Al-rich fusion zone (Fig. 2f, g). Moreover, keyhole mode welding has revealed the presence of micro-cracks and defects within the weld and in proximity to the gap between the sheets (see Fig. 1). The HAZ varies significantly from the steel to the Al-side, including the formation of $FeAl_3$ eutectic phase through solid-state Fe diffusion into the Al (Fig. 1).

Electrochemical evaluation

AEN (Asymmetric Electrochemical Noise). Figures 3a, b present the open circuit potential (OCP) and zero resistance ammeter (ZRA) results with immersion times in 0.6 M NaCl solution, respectively. It is known that OCP and ZRA fluctuate with time as a result of corrosion evolutions such as pitting initiation, pitting propagation, and repassivation[17–19]. The region where OCP oscillation occurred at the early stage of the measurement would be associated with pitting propagation and the OCP oscillation was observed for all cases, indicating passivity loss leading to pitting initiation. The OCP results indicate a decrease in the potential of all samples after 2000 s of immersion, which could be attributed to the formation of oxide layers on the samples, subsequently reducing their nobility[20]. Subsequent to this period, the potential values were observed to remain stable, indicative of the establishment of a steady thermodynamic corrosion system[17]. Notably, the similarity in sample potential values suggests that the weld minimally impacted the thermodynamic stability of the system during the two-hour immersion period.

In Fig. 3b, the ZRA result demonstrates a decrease in current density across all samples over time, reflecting a stable kinetic system. Particularly, the non-welded steel to Al interface exhibited a significant reduction in current density compared to the welds, suggesting the presence of oxides and their inhibitory effect on oxidative element access (e.g., water and oxygen) to the exposed materials[20,21]. Conversely, the presence of cracks, IMCs, and voids in the welds hindered the stability of the native passive film on the surface[22]. Additionally, all welds displayed a lower current density than the non-welded regions, indicating reduced chemical activity due to the formation of an intermediate alloy between steel and Al[19,23,24]. The presence of η-Fe_2Al_5 IMC mitigates the detrimental cathodic effect of IF steel on the

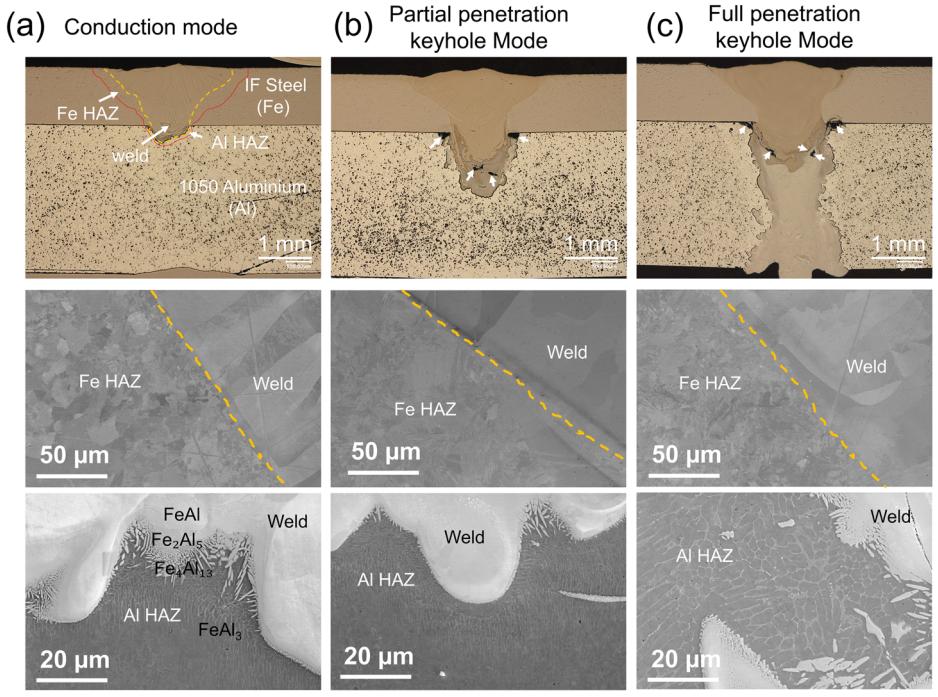

Fig. 1 | Overview of the conduction and keyhole mode dissimilar weld microstructures. Optical micrographs **a** conduction, **b** partial penetration keyhole and **c** full penetration keyhole mode. Arrows in figures **b** and **c** indicate the presence of micro-cracks and defects. SEM images displaying the heat-affected zone (HAZ) and IMCs.

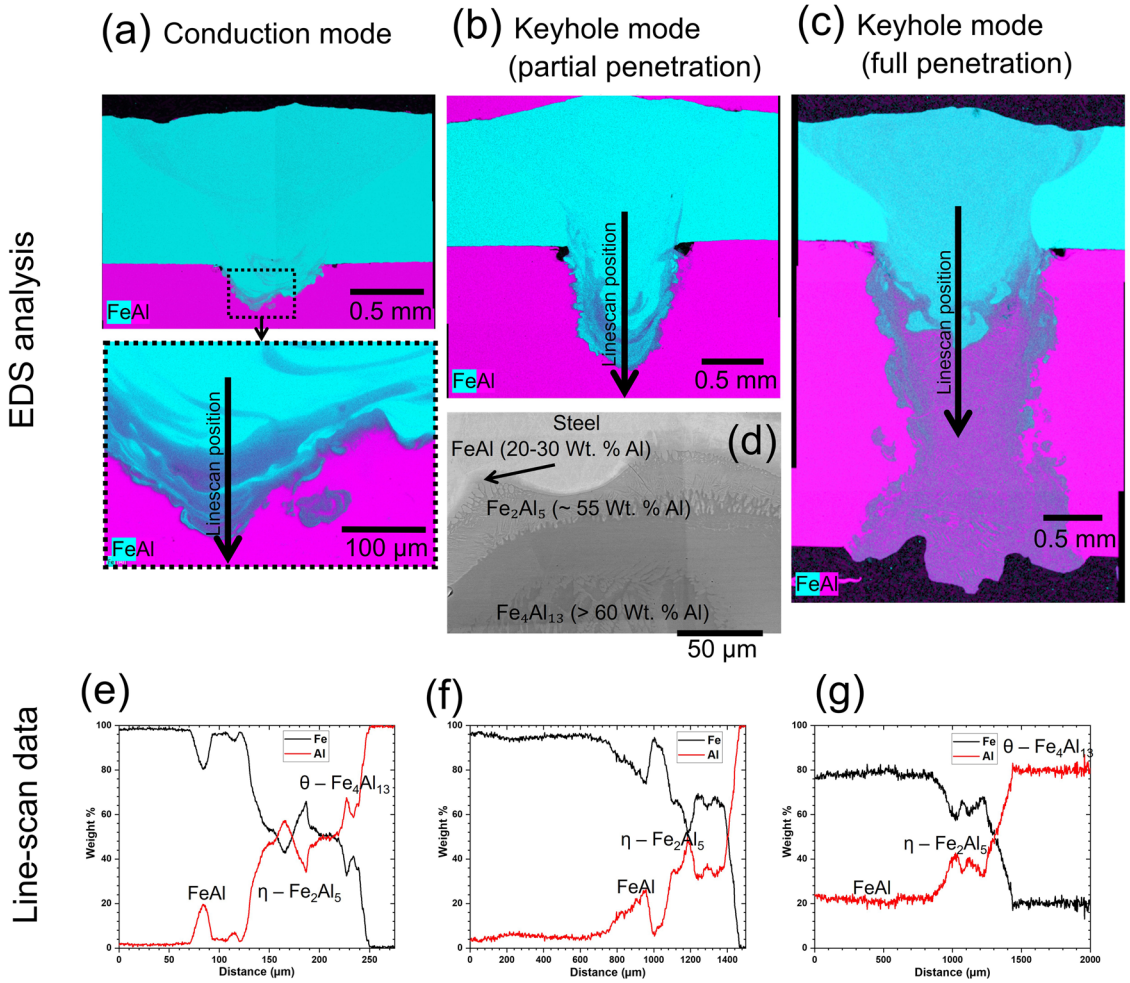

Fig. 2 | SEM-EDS chemical maps showing the metal mixing between Fe and Al. Showing the **a** conduction, **b** partial penetration keyhole and **c** full penetration keyhole mode welds, with corresponding line-scans – **e**–**g**, respectively. High resolution SEM-BSE image of IMC types is shown in **d**.

Fig. 3 | AEN testing results. Samples were immersed for 2 hours in 0.6 M NaCl: **a** OCP and **b** ZRA.

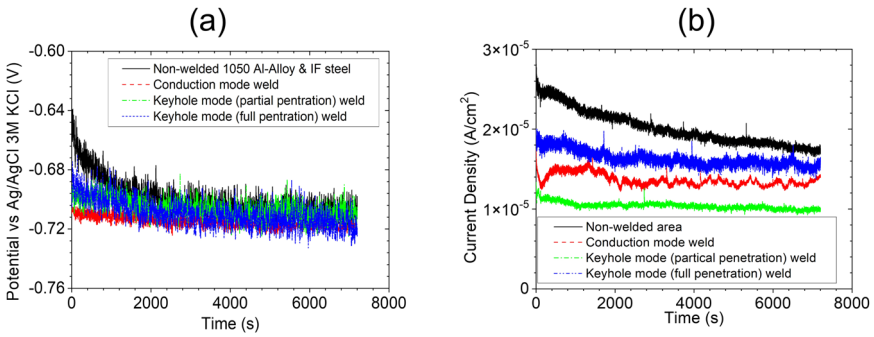

1050 Al alloy. This occurs because η-Fe_2Al_5 exhibits a higher corrosion potential (−0.35 V vs Ag/AgCl) compared to the steel (−0.5 V vs Ag/AgCl). This difference in potential leads to the galvanic oxidation of IF steel by η-Fe_2Al_5, thereby reducing the steel's ability to act as a cathode relative to the Al. This phenomenon aligns with observations reported by De Graeve et al.[25] and Lemmens et al.[26] on coated steel. While $FeAl_3$ also has a cathodic effect on the Al matrix, its negative impact is likely less significant due to its similar potential to steel (−0.505 V vs Ag/AgCl)[27].

The non-welded sample had the highest current density, followed by full penetration keyhole, conduction mode, and finally partial penetration keyhole welding (which exhibited the lowest). This order reflects the type and distribution of IMCs formed. The cathodic nature of θ-Fe_4Al_{13} (≈ −0.5 V vs Ag/AgCl), relative to the Al alloy (≈ −1 V vs Ag/AgCl)[22,26], drives accelerated corrosion. Therefore, the reduction of θ-Fe_4Al_{13} in partial penetration keyhole welding explains its lower current density. In contrast, β-FeAl (≈ −1 V vs Ag/AgCl)[28]) has a similar potential to the Al alloy, resulting in a negligible impact on corrosion resistance.

AEN features (e.g., current density root mean square, asymmetric electrochemical noise resistance, and localised index) of the samples are listed in Table 1. The current density root mean squares ($I_{R.M.S.}$) were

Table 1 | AEN features of the non-welded and welded and samples for 2 hours of immersion in 0.6 M NaCl

Sample	$I_{R.M.S.}$ (A/cm²)	σ_I (A/cm²)	σ_E (V)	R_{AEN} (Ω×cm²)	*L.I.*
Non-welded 1050 Al alloy & IF steel	2.025×10^{-5}	2.027×10^{-4}	0.120	55.370	0.10
Conduction mode	1.368×10^{-5}	7.345×10^{-5}	0.349	47.580	0.05
Partial penetration keyhole mode	1.193×10^{-5}	1.084×10^{-4}	0.085	78.040	0.09
Full penetration keyhole mode	1.635×10^{-5}	5.628×10^{-4}	0.444	78.930	0.03

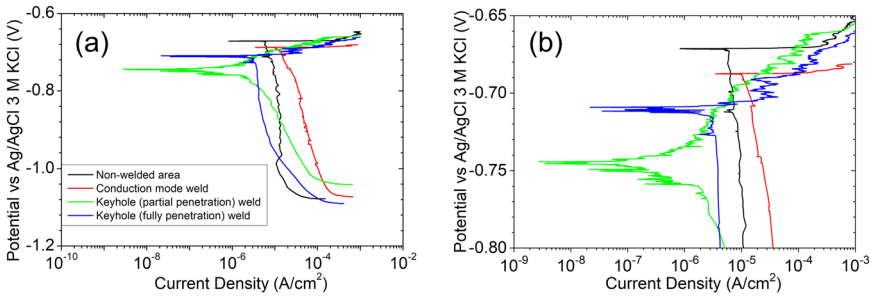

Fig. 4 | PPC results. Samples were immersed for 2 hours in 0.6 M NaCl **a** overall curve and **b** intersect area of the anodic and cathodic branch.

calculated with Eq. (1)[22].

$$I_{R.M.S} = \sqrt{\frac{\sum_i^N I_i^2}{N}} \quad (1)$$

Where, I_i is the current density per measurement and N is the measurement number. The samples had similar $I_{R.M.S.}$ with one another. The same behaviour was observed for asymmetric electrochemical noise resistance (R_{AEN}), being estimated with Eq. (2)[29].

$$R_{AEN} = \frac{\sigma_E}{\sigma_I} \quad (2)$$

Here, σ_E and σ_I were potential and current density standard deviations, respectively. All samples showed a mixed corrosion mechanism (localised and general) as showing the localised index (*L.I.*), which was calculated with Eq. (3)[23].

$$L.I. = \frac{\sigma_I}{I_{R.M.S.}} \quad (3)$$

For values ≥ 0.1, the corrosion process is localised; between 0.1 to 0.01, it is mixed; and for values less 0.01 it is general. The breakdown of the passive film on the metal surface exposes the underlying metal to the corrosive environment, initiating simultaneous anodic and cathodic reactions. This concurrent occurrence of metal dissolution (anodic) and reduction reactions (cathodic) is characteristic of a mixed corrosion mechanism[23].

PPC (Potentiodynamic Polarisation Curves). Figure 4 illustrates the PPC results. Most of the samples exhibited distinctive cathodic and anodic branches. All samples had a horizontal curve at low potential (≈−1.1 V vs Ag/$AgCl_3$ M KCl) due to the evolution of the water and oxygen[25]. The vertical curve of the cathodic branch showed a reduction reaction controlled by diffusion[21,23,30,31]. Furthermore, all of the welded samples presented fluctuation of the cathodic branch due to the activation and deactivation processes. The fluctuations observed are likely due to metastable pitting events caused by the Al_xFe_y IMC present within the Al matrix. This IMC, being anodic with respect to the surrounding matrix, acts as a preferential site for localised corrosion initiation. The breakdown and repassivation of the passive film on these IMC particles lead to observed fluctuations in the electrochemical signal[22,32,33]. The only exception was the full penetration keyhole mode welding. The horizontal curve of the anodic branch signified the high activity of the oxidation reactions[21,31]. The partial penetration keyhole mode welded sample however demonstrated a different PPC shape characterised by inclined curves, indicating mixed control for cathodic and anodic reactions[31]. This variation in corrosion performance can be attributed to the weld composition. Specifically, lower quantities of θ-Fe_4Al_{13}[34] and the increased presence of finer IMCs[21] reduce the overall chemical activity of the joint. This mitigates the negative impact of the decreased anodic effect on the Al matrix. While θ-Fe_4Al_{13} significantly accelerates corrosion, the influence of β-AlFe on the 1050 Al alloy is minimal. Further, η-Fe_2Al_5 can reduce the IF steel's cathodic effect on the Al[26]. Note that η-Fe_2Al_5 and β-AlFe are present in all welded samples. The keyhole partial and full penetration samples exhibited fluctuations in the anodic branch of their polarization curves. These fluctuations are also attributed to metastable pitting events, but in contrast to the previous case, they are caused by the presence of IMCs with a cathodic effect on the Al matrix, specifically $FeAl_3$, and θ-Fe_4Al_{13}. These IMCs, being cathodic relative to the surrounding matrix, create localised galvanic couples that can lead to the breakdown and repassivation of the passive film on the Al, resulting in the observed fluctuations[19,35]. Fluctuations in the cathodic branch were absent in both non-welded and conduction welded samples due to the high susceptibility of the passive film to breakdown, which hinders its re-passivation. In the non-welded samples, the IF steel exerts an unmitigated cathodic effect on the Al matrix because of the absence of the η-Fe_2Al_5 phase. This increased cathodic influence promotes the breakdown of the passive film, preventing it from reforming effectively[25]. In conduction welded samples, the increased size and concentration of the $FeAl_3$ and θ-Fe_4Al_{13} IMCs exacerbate the breakdown of the passive film. The cathodic effect of these IMCs intensifies with their growing size and volume, contributing to a more pronounced susceptibility to corrosion[21].

The corrosion characteristics from PPC testing are presented in Table 2. Comparable corrosion current densities (I_{corr}) and diffusion (I_{diff}) across three samples indicated that diffusion processes primarily controlled their corrosion rates[31]. Specifically, for the partial penetration keyhole mode welding, the I_{diff} calculation was impractical due to the mixed control of the cathodic branch. In this case, I_{corr} emerged as the dominant kinetic factor, therefore, this sample showed a lower corrosion rate. The observed improvement in corrosion resistance can be attributed to the reduced cathodic effect of Fe on Al in the absence of a continuous IMC layer[34]. The reducing presence of θ-Fe_4Al_{13} is particularly significant because it directly promotes cathodic behaviour on the Al surface[26]. This reduction in chemical activity enhanced

Table 2 | PPC characteristics of the samples

Sample	I_{corr} (A/cm^2)	I_{diff} (A/cm^2)	E_{corr} (V)
Non-welded 1050 Al alloy & IF steel	8.032×10^{-6}	1.250×10^{-5}	−0.671
Conduction mode	1.026×10^{-5}	1.545×10^{-5}	−0.723
Partial penetration keyhole mode	1.028×10^{-6}	–	−0.744
Full penetration keyhole mode	6.023×10^{-6}	6.103×10^{-6}	−0.709

the weld's corrosion resistance. The estimation of I_{corr} was based on Tafel lines interception[36]. Additionally, the corrosion potential (E_{corr}) values for all samples were nearly identical, differing by less than 0.08 V, emphasising the welding area only influenced the kinetics of the corrosion. It is important to note that the passive film breakdown potential was not observed in the PPC because it coincided with the corrosion potential[16,37].

EIS (Electrochemical Impedance Spectroscopy). Evaluation of the corrosion mechanisms over time was conducted using EIS, illustrated in Nyquist and Bode plots (Fig. 5). The assessment of corrosion processes at specific time constants was performed using the equivalent circuit method. Particularly, distinct corrosion mechanisms were observed through EIS results across all samples as time progressed (Fig. 5). Consequently, four distinct equivalent circuits were proposed based on the EIS results to represent the corrosion mechanisms (Fig. 6).

The initial equivalent circuit (Fig. 6a) was constructed based on five-time constants. The first-time constant appeared as a flat line at the highest frequency (10^5 Hz) in the Bode plots of impedance modulus (Z_{mod}) concerning frequency (F). This indicated that this element is a resistance (R_1)[38]. The second time constant was observed as a loop at low real impedance (Z_{real}) in the Nyquist plots, a curved pattern in Z_{mod} vs F, and a peak in phase angle (θ) concerning F at a high-frequency range (10^4–10^5 Hz) in Bode plots[38]. This second time constant was comprised of a parallel resistance (R_2) and a constant phase element (CPE_2 and n_2) in series with the first time constant.

The third- and fourth-time constants were depicted using the same element as the preceding first circuit element, involving R_3, CPE_3, n_3 (third-time constant), and R_4, CPE_4, n_4 (fourth-time constant). These elements were connected in series with R_1, while the constant phase elements were linked in series with the preceding resistances (R_2 with CPE_3 and R_3 with CPE_4). Both time constants appeared as flattened loops at the midpoint Z_{real} and as rounded peaks at the intermediate frequency range (10^{-1}–10^4 Hz) in Nyquist and Bode (θ vs F) plots, respectively. In the other Bode plot (Z_{mod} vs F), an inclined curve with two slopes from 10^{-1} Hz to 10^4 Hz was observed, indicating a significant overlap between the time constants. Notably, certain EIS plots display a flat or dual peak, signifying reduced overlap[38,39].

The final time constant was indicated by a negative loop in the Nyquist plot and negative slopes in both Bode plots at the low-frequency range (10^{-2}-10^{-1} Hz), representing a composite of a resistance (R_5) in series with an inductor (L_5) signifying the adsorption-desorption process[39]. These elements were in series with R_1 and in parallel with the other elements of the time constant. Notably, this particular equivalent circuit has been observed in previous literature[40].

The second equivalent circuit (Fig. 6b) closely resembled the previous one, except for the absence of the second time constant. Additionally, a new time constant of adsorption-desorption (L_6 and R_6) was introduced, linked in series with R_1 and in parallel with the other elements. This new time constant, signifying the adsorption-desorption process, manifested as a pronounced negative loop[41]. This equivalent circuit has been utilised in other research studies[40].

The third equivalent circuit (Fig. 6c) retained the same resistances and constant phase elements as the previous equivalent circuit, excluding the adsorption-desorption time constants (L_5, L_6, R_5, and R_6). Another time constant, namely Warburg impedance, was added in series with R_4 to represent the diffusion process[23,38,41,42]. This equivalent circuit has been applied in various other studies[17,23,43].

The final equivalent circuit (Fig. 6d) mirrored the preceding equivalent circuit, but with the addition of the second time constant in a similar position as in the initial equivalent circuit. This equivalent circuit has been identified in existing literature[40].

The corrosion mechanisms, represented through equivalent circuits, were observed in the samples based on immersion time and type (Fig. 5), detailed in Table 3. Variation in the equivalent circuits over immersion time for the same sample indicated the evolution of the sample's corrosion mechanisms over time.

The Bode and Nyquist plot equivalent circuits exhibited a favourable agreement with the experimental data (Fig. 7), confirmed by acceptable chi-square values (X^2) ranging from 10^{-3} to 10^{-2}, validating the suitability of the data simulated with equivalent circuits. R_1 maintained values around Ωcm^2 for all samples and immersion times, representing the dissolution resistance[44]. Other equivalent circuit elements varied over time, displaying diverse behaviours based on the sample, as outlined in Table 4.

For the ***non-welded region***, the second time constant indicated a reduction in resistance over time, signifying a decline in corrosion resistance[23]. CPE_2 fluctuated over time, reducing for 24 hours of immersion or less, increasing from 24 hours to 72 hours, and then reducing between 72 hours and 96 hours, implying a thickness fluctuation of the corrosion evolution[45]. Similarly, n_2 revealed fluctuations over time, indicating surface damage and repair during testing, influenced by the surface condition, with lower values corresponding to higher roughness or damage[43,46]. The third time constant displayed a decreasing resistance (R_3) over time, except at 96 hours, where R_3 increased. Conversely, CPE_3 showed an opposite trend to R_3, suggesting that resistance increments were due to process thickening, while reductions were related to process thinning[45]. Similarly, n_3 fluctuated over time similarly to the previous time constant. R_4 (fourth time constant) increased after 24 hours of immersion, remaining constant for longer immersion times. CPE_4 decreased over time, indicating a thickness and corrosion resistance increase[23,45]. Notably, n_4 remained constant around 1, over time. Warburg impedance maintained a consistent value around 10^{-3} $Ss^{-0.5}cm^{-2}$ for all immersion times, indicating that diffusion processes remained constant over time[40]. Overall, this data suggests that the corrosion resistance of the samples decreases with immersion time from 24 hours to 72 hours, however, slightly higher at 2 hours and 96 hours.

For the ***conduction mode weld***, CPE_2 and n_2 (second time-constant) remained stable over time, while R_2 decreased, suggesting a reduction in corrosion resistance without changes in thickness and surface status[45]. R_3 fluctuated over time, while CPE_3 decreased (third time-constant), indicating an increase in process thickness over time without a clear resistance increment[23]. n_4 oscillated between 0.7 and 0.8 with immersion time. The fourth time-constant exhibited fluctuating CPE_4, increasing R_4 over time, while n_4 remained approximately 1, indicating corrosion resistance rise over time for this process. Warburg impedance maintained a constant value around 2×10^{-6} $Ss^{-0.5}cm^{-2}$, implying constant diffusion processes over the immersion time[43]. These findings suggest an increase in corrosion resistance in the sample over time.

For the ***partial penetration keyhole mode weld***, CPE_2 increased over time, while n_2 decreased (second time constant), indicating thinning and damage to the second time constant process with time[43,47]. R_2, however, remained constant over time. R_3 decreased over time, while n_3 increased and CPE_3 remained within the range of 10^{-5} $Ss^{-0.5}cm^{-2}$ (third time constant), signifying a decrease in corrosion resistance[43] with constant thickness[23] and surface flattening over time[43]. The element values for the fourth- and fifth-time constants remained constant over time, with Warburg impedance similar to that of the other samples. These findings collectively suggest a general decrease in corrosion resistance but stay to be higher than other weld samples.

For the ***full penetration keyhole mode weld***, the second time constant demonstrated a decrease in R_2 and CPE_2 over time, while n_2 remained constant, this indicates a reduction in corrosion resistance during the

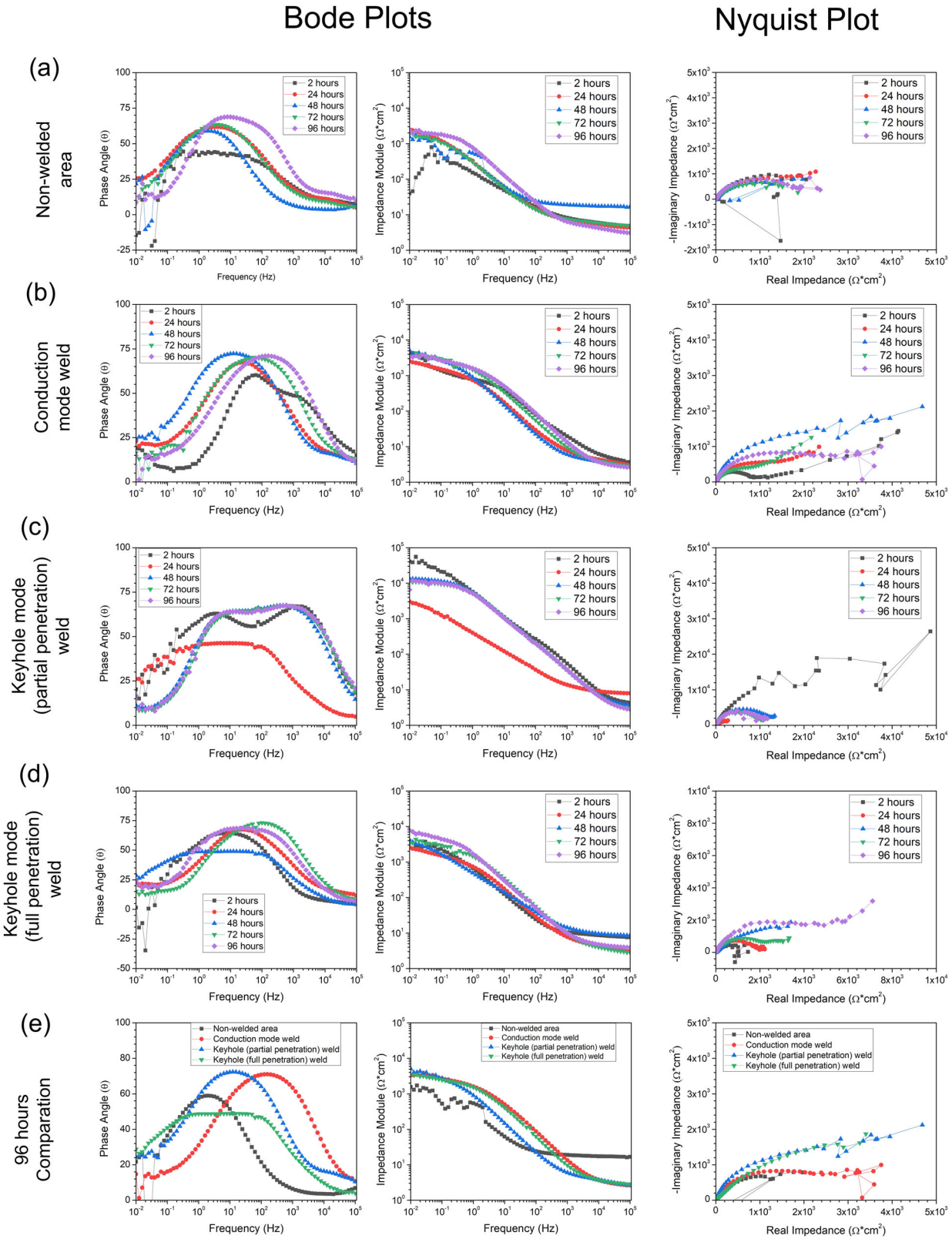

Fig. 5 | Bode and Nyquist plots (EIS Data). For **a** non-welded 1050 Al alloy/ IF steel areal, **b** conduction mode weld, **c** keyhole mode (partial penetration) weld, **d** keyhole mode (full penetration) weld, immersed for 2, 24, 48, 72, and 96 hours. Figure **e** represents the comparative results of all four samples for the 96-hour immersion test.

process[43] with an increase in thickness[47]. Similar trends were observed for the elements of the third time constant. The corrosion resistance for the fourth time constant increased over time, evidenced by the reduction in CPE_4 and increase in R_4[48]. n_4 also fluctuated over time, indicating a cyclic process of surface damage and recovery over time. The diffusion process remained constant over time, signified by the invariable Warburg impedance[47]. R_5 remained constant over time, while L_5 decreased (fifth time constant), implying a reduction in the frequencies of the adsorption-

desorption process[23]. This data collectively suggests an increase in corrosion resistance over time.

Across all samples and immersion times, the resistance R_4 was the primary factor influencing corrosion resistance, with the highest values offering the best protection. Partial penetration keyhole welding exhibited the highest R_4, followed by full penetration keyhole, conduction mode welding, and finally the non-welded 1050 Al alloy and IF steel (which had similar R_4 values).

This order reflects the type, shape, and distribution of IMCs. The absence of a continuous θ-Fe_4Al_{13} layer significantly enhances the R_4 of the partial penetration sample due to the reduced cathodic effect of this IMC on the Al[26]. Although present, the smaller and less numerous θ-Fe_4Al_{13} IMCs in the full penetration weld also reduce the cathodic effect[21,34] A similar effect occurs with $FeAl_3$ in the HAZ. Finally, the increased η-Fe_2Al_5 in this weld configuration may further mitigate the cathodic action of the IF steel, contributing to its higher R_4 compared to conduction mode welding[25]. Overall, the presence of IMCs strongly influences the resistance values obtained from EIS.

The complexity of the equivalent circuit arises from the multi-material nature of the corrosion system, comprising two materials in non-welded samples (1050 Al-alloy and IF steel) and three in welded samples (with the addition of the IMCs in weld). Each material exhibits its own distinct corrosion processes, and interactions between these materials can further influence the overall electrochemical behaviour. These individual and interactive corrosion processes, which contribute to the complexity of the equivalent circuit model, are detailed in the discussion.

Analysis of microstructures in corroded samples

Figures 8 and 9 display a comprehensive SEM and EDS analysis of the samples post-PPC test exposure. Figure 8 presents a cross-section (side view) analysis of the non-welded region and welds to facilitate the evaluation of pitting, depth, and the type of corrosion. These microstructural findings suggested that the presence of IMCs in the weld intensify the susceptibility of the Al to GC, aligning with the electrochemical results. Varied degrees of micro-galvanic corrosion are observed at different interfaces of the weld (HAZs at Al- and steel-side, weld-gap), within the weld, and the non-welded region.

Figure 12 presents a typical scenario of polygonal corrosion observed on the Al-side, excluding the weld region. However, when Fe becomes nobler (more cathodic) than Al, pitting corrosion developed on the Al surface. The corrosion products on the steel-side are primarily Fe and O (e.g., Fe_2O_3), while the Al surface is mainly composed of Al and O oxides (e.g., Al $(OH)_3$, Al_2O_3). Within the Al matrix, pitting corrosion initiates around Fe_3Al IMC due to their cathodic nature[49–52]. In essence, the IMCs form a galvanic couple with the Al matrix, acting as the cathode and accelerating the oxidation and dissolution of Al in the surrounding area. Over time, this process leads to the detachment of IMCs from the Al matrix, resulting in the observed pitting[53,54]. Notably, β-AlFe has minimal influence on pitting corrosion because its electrochemical potential is similar to that of the Al matrix. As a rule, GC is proportional to the difference in the corrosion potentials of the involved materials[32,55].

Around the weld gap, the corrosion product mainly consists of Al, Fe, and O. This mixed corrosion product includes $Fe_2O_3{\cdot}nH_2O$/ FeO (OH)/ $Fe(OH)_3/FeCl_3$, and $Al_2O_3/Al(OH)_3/AlCl_3$. Cathodic and anodic reactions explain in Eqs. (4)–(7)[56–59]:

$$\text{Anodic}: Fe \rightarrow Fe^{+2} + 2e^- \quad (4)$$

$$\text{Anodic}: Al \rightarrow Al^{+3} + 3e^- \quad (5)$$

$$\text{Cathodic}: 2H_2O + O_2 + 4e^- \rightarrow 4OH^- \quad (6)$$

$$\text{Cathodic}: 2H_2O + 2e^- \rightarrow 2OH^- + H_2 \quad (7)$$

Corrosion product formation reactions explain in Eqs. (8)–(13)[56–59]:

$$4Fe(OH)_2 + O_2 \rightarrow 2Fe_2O_3 + 4H_2O \quad (8)$$

$$Fe_2O_3.nH_2O \leftrightarrow 2FeO(OH) + (n-1)H_2O \leftrightarrow 2Fe(OH)_3 + (n-2)H_2O \quad (9)$$

$$Fe(OH)_3 + 3Cl^- \leftrightarrow FeCl_3 + 3(OH^-) \quad (10)$$

$$2Al(OH)_3 \leftrightarrow Al_2O_3 + 3H_2O \quad (11)$$

$$Al + 2H_2O + 2OH^- \leftrightarrow Al(OH)_4^- + 3H_2 \quad (12)$$

$$Al(OH)_3 + 3Cl^- \leftrightarrow AlCl_3 + 3OH^- \quad (13)$$

The SEM analysis using EDS findings of the weld microstructure indicates that micro-GC primarily occurs around the coarse cathodic IMCs

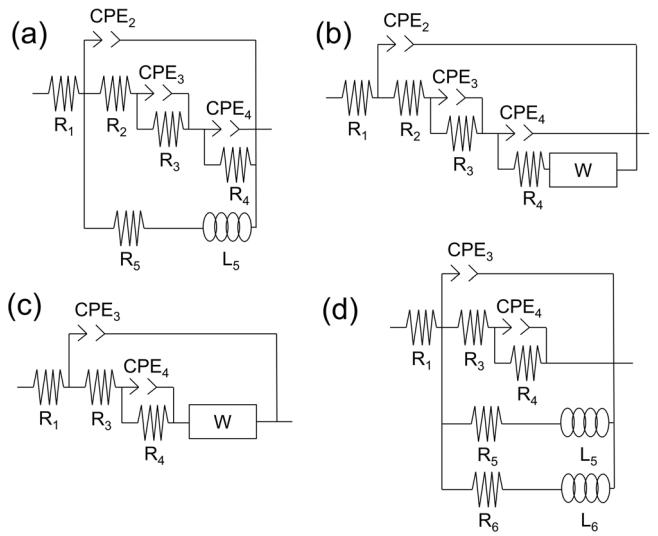

Fig. 6 | The equivalent circuits. Schematics equivalent circuits (**a**–**d**) proposed using EIS results to represent the corrosion mechanisms of the samples.

Table 3 | Equivalent circuits of the samples according to immersion time

Immersion time (h)	Sample			
	Non-welded 1050 & IF steel	Conduction mode	Keyhole mode (partial penetration)	Keyhole mode (full penetration)
2	First	Third	Fourth	Second
24	Fourth	Fourth	Fourth	First
48	Fourth	Fourth	Third	Fourth
72	Fourth	Fourth	Third	Fourth
96	Fourth	Third	Third	Third

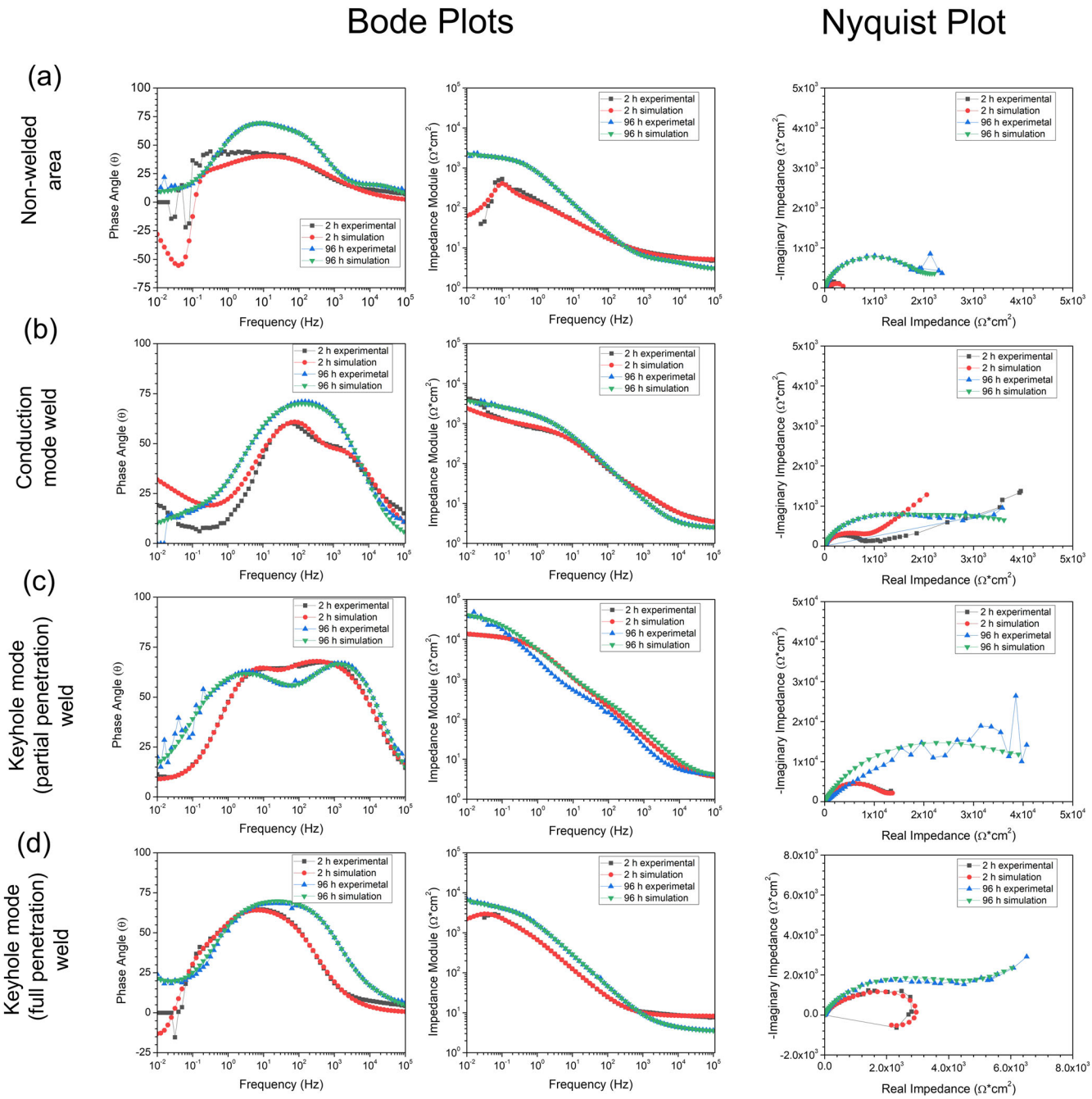

Fig. 7 | Comparison (equivalent circuit and experimental results) of Bode and Nyquist plots. Utilising equivalent circuit and experimental results for **a** non-welded 1050 Al alloy/IF steel area, **b** conduction mode weld, **c** keyhole mode (partial penetration) weld, and **d** keyhole mode (full penetration) weld.

like η-Fe_2Al_5 and θ-Fe_4Al_{13} present at the Al interface. In contrast, during keyhole mode welding, the η-Fe_2Al_5 and θ-Fe_4Al_{13} IMC layer is discontinuous along the Al/weld interface, with coarse IMCs primarily concentrated near the gap between the sheets. This region exhibits large pitting. In the case of the full penetration mode weld, the IMCs are distributed throughout the weld without a continuous layer, resulting in improved corrosion resistance and the occurrence of individual pitting in specific locations. The large area fraction of the cathodic element (η-Fe_2Al_5 and θ-Fe_4Al_{13}) encourage GC[56]. Moreover, the welds exhibit significant variations in chemical composition within each weld and across the three different welds. Additionally, these welds display defects such as solidification and cold-cracking, which further contribute to localised corrosion[5]. Regions at the weld pool bottom, where IMCs are coarser, exhibit deeper pitting compared to areas of finer IMCs. Additionally, weld cracks, common at the weld pool bottom or near the gap, can further accelerate localized corrosion by serving as pitting initiation sites[5]. This is attributed to the cracks providing a pathway for corrosive agents to reach the underlying metal. Additionally, within welds, GC was observed, leading to the dissolution of the matrix around the IMCs.

Numerous pits are visible in the HAZs on both the Al- and steel- sides. The size of the pits is notably larger on the Al-side of the HAZ, suggesting that the Al-side HAZ exhibits the weakest pitting corrosion resistance among all three weld samples. The pitting was concentrated around the eutectic $FeAl_3$ region within the primary Al grains. On the steel-side of the coarse-grained HAZ, the initiation of pitting corrosion is primarily attributed to the altered ferritic microstructure, the accumulation of dislocations, and the presence of residual stresses, all of which serve as nucleation sites for pitting corrosion. θ-Fe_4Al_{13} accelerates IF steel corrosion due to its significantly higher electrochemical potential[25].

Table 4 | Values of the equivalent circuit values of the sample's corrosion mechanisms according to immersion time in 0.6 M NaCl

Non-welded 1050 Al alloy & IF steel																
Time (h)	R_1 (Ωcm^2)	R_2 (Ωcm^2)	CPE_2 ($Ss^{-n}cm^{-2}$)	n_2	R_3 (Ωcm^2)	CPE_3 ($Ss^{-n}cm^{-2}$)	n_3	R_4 (Ωcm^2)	CPE_4 ($Ss^{-n}cm^{-2}$)	n_4	W ($Ss^{-0.5}cm^{-2}$)	L_5 (Hcm^2)	R_5 (Ωcm^2)	L_6 (Hcm^2)	R_6 (Ωcm^2)	X^2 (10^{-3})
2	6.000	588.1	0.001	0.55	954.5	1.123×10^{-7}	0.53	84.5	0.002	1.00	-	852.96	954.48	-	-	72.80
24	7.151	3.9	1.780×10^{-7}	0.86	36.7	3.230×10^{-4}	0.74	3500.4	1.090×10^{-4}	0.77	2.320×10^{-4}	-	-	-	-	1.19
48	9.588	5.4	1.960×10^{-6}	0.80	5.5	2.380×10^{-4}	0.84	1320.6	6.380×10^{-4}	0.75	0.006	-	-	-	-	1.48
72	7.956	5.2	1.440×10^{-4}	0.68	73.8	2.670×10^{-4}	0.74	2992.8	3.840×10^{-4}	0.94	0.010	-	-	-	-	1.71
96	4.744	5.3	3.900×10^{-5}	0.77	328.3	7.460×10^{-5}	0.88	2907.6	2.070×10^{-5}	0.94	0.005	-	-	-	-	1.75
Conduction mode welding																
2	3.320	-	-	-	77.7	8.310×10^{-5}	0.72	817.0	6.640×10^{-6}	1.00	0.002	-	-	-	-	32.90
24	2.592	11.1	6.780×10^{-6}	0.93	39.9	2.020×10^{-4}	0.77	1256.4	1.030×10^{-4}	1.00	0.003	-	-	-	-	1.74
48	2.335	2.3	2.850×10^{-5}	0.85	732.0	1.900×10^{-4}	0.84	1946.4	2.510×10^{-6}	1.00	0.001	-	-	-	-	1.43
72	2.444	1.5	5.940×10^{-6}	0.93	12.5	9.750×10^{-5}	0.78	2800.0	1.830×10^{-6}	1.00	0.003	-	-	-	-	2.07
96	2.476	-	-	-	1526.4	5.910×10^{-5}	0.86	3314.4	6.370×10^{-4}	0.96	0.003	-	-	-	-	1.47
Keyhole partial penetration welding																
2	3.761	435.2	1.080×10^{-5}	0.85	32593.0	3.220×10^{-5}	0.72	8574.5	2.490×10^{-7}	0.78	5.930×10^{-4}	-	-	-	-	4.79
24	7.725	636.0	6.050×10^{-4}	0.61	3947.9	$3.430 \times 10^{-4.}$	0.57	10.3	2.200×10^{-3}	0.95	0.009	-	-	-	-	1.71
48	3.332	-	-	-	1272.7	2.420×10^{-5}	0.81	10695.3	8.710×10^{-6}	0.84	0.001	-	-	-	-	1.18
72	2.491	-	-	-	1207.8	2.560×10^{-5}	0.80	8825.3	7.730×10^{-6}	0.85	0.002	-	-	-	-	1.19
96	2.304	-	-	-	1158.3	2.610×10^{-5}	0.80	9341.2	7.660×10^{-6}	0.89	0.002	-	-	-	-	1.28
Keyhole full penetration welding																
2	8.237	-	-	-	4058.5	3.400×10^{-4}	0.77	2996.3	4.340×10^{-4}	1.00	-	854.9	7716.2	3431.0	51269.4	2.53
24	3.117	1997.6	6.610×10^{-4}	0.82	406.9	1.500×10^{-4}	0.86	1362.9	1.070×10^{-4}	0.67	-	29.4	7023.5	-	-	2.29
48	7.536	27.357	5.100×10^{-4}	0.62	759.5	9.050×10^{-6}	0.92	3032.7	2.060×10^{-4}	0.79	0.003	-	-	-	-	0.18
72	2.493	5.6188	7.050×10^{-5}	0.81	1478.4	7.170×10^{-6}	0.99	3678.4	8.850×10^{-4}	0.63	0.003	-	-	-	-	0.81
96	3.441	-	-	-	3.074	5.490×10^{-5}	0.82	4435.2	6.300×10^{-5}	0.81	0.001	-	-	-	-	1.44

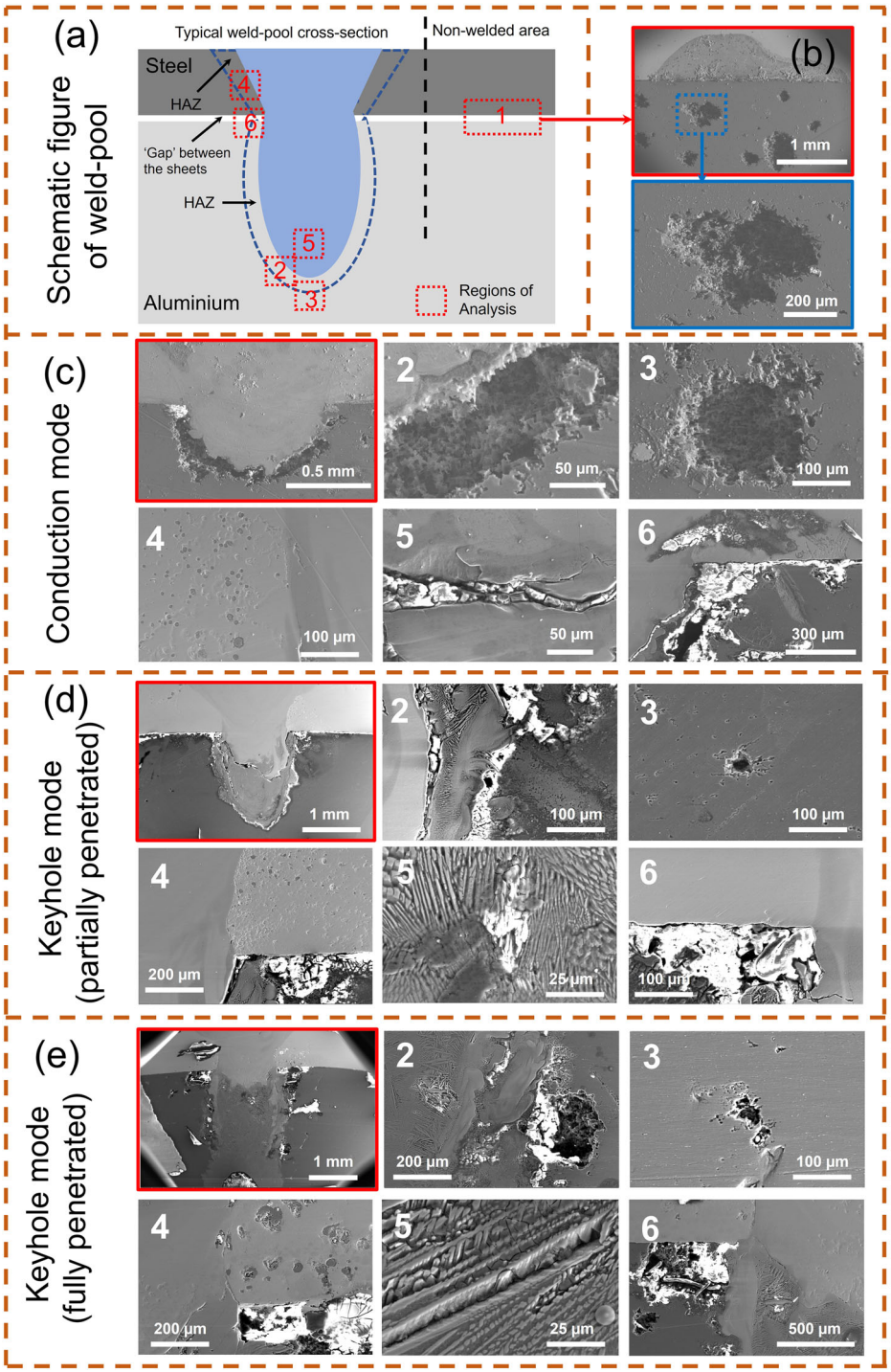

Fig. 8 | Microstructural images after PPC analysis. Schematic diagram of weld with region **a** of analysis (**1** – non-welded area, **2** – Al/weld interface, **3** – HAZ Al-side, **4** – HAZ steel-side, **5** – within weld, **6** – gap between the sheets), **b** non-welded area, **c** conduction mode weld, **d** keyhole mode (partial penetration) weld, and **e** keyhole mode (full penetration) weld. High-magnification microstructures (**2–6**) are included with each weld.

Discussion

The corrosion attributes of dissimilar metal welds are notably affected by different microstructural characteristics, encompassing the type, size, and distribution of IMCs, chemical segregation, HAZ, and any existing defects. The findings mentioned in the results indicate an asymmetric response in corrosion resistance at different interfaces of the weld microstructure, suggesting the presence of distinct corrosion mechanisms over time, as discussed below.

Based on the findings from electrochemical tests and microstructural analysis, it was observed that localised corrosion around the coarse needle-shaped directionally grown η-Fe_2Al_5 and θ-Fe_4Al_{13} IMC is more pronounced, particularly when it forms a continuous layer in the Al-side (conduction mode). The potential difference between the IMC (cathodic) and Al (anodic) leads to GC and the developed extensive, continuous pitting along the Al/weld interface[49–52] η-Fe_2A_{l5} mitigates the harmful cathodic effect of IF steel on the Al matrix, thereby enhancing corrosion resistance[25,60]. This stands in contrast to the surface of the weld or the various distributions in the keyhole (partial and full penetration) mode welds. IMCs with cathodic effects promotes the breakdown of the passive film of the Al, producing a passive breaking film equal to corrosion potential[61]. This is only observed in the PPC anodic branch. Thus, the absences of the fluctuations in the cathodic branch for full penetration keyhole mode welding, indicates that this weld reduces the anodic effect of the IMCs in the matrix.

Both the conduction and full penetration welds displayed a corrosion mechanism primarily governed by diffusion, as indicated by the similar

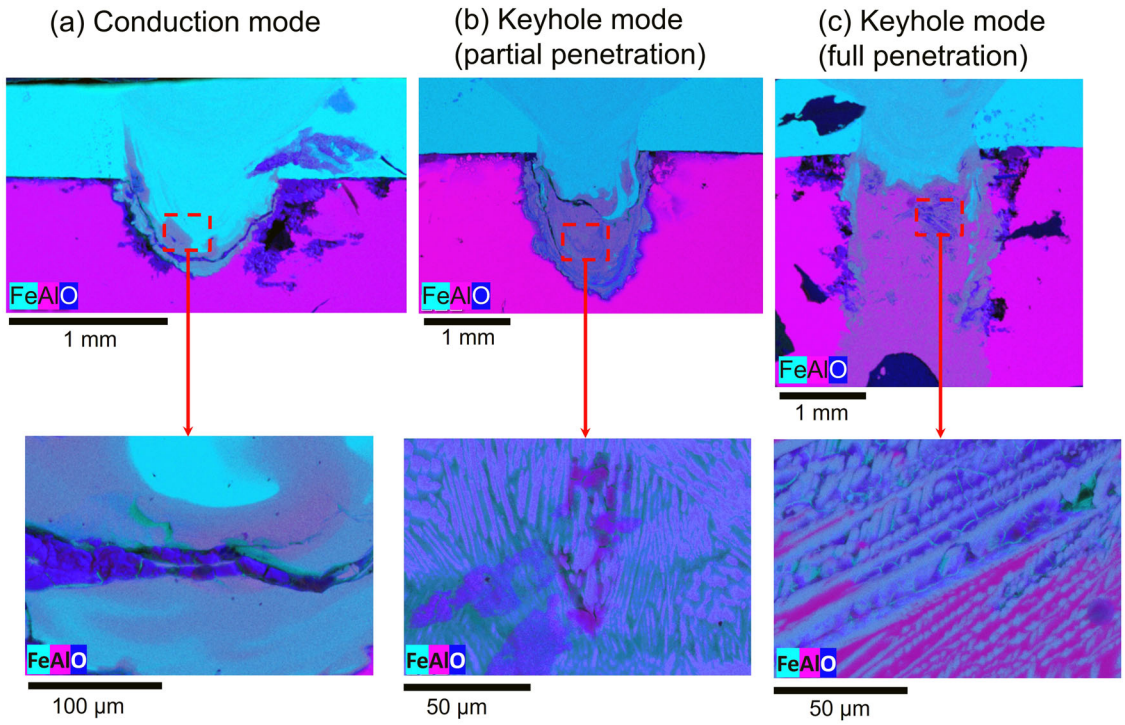

Fig. 9 | SEM-EDS analysis of weld after PPC test. Showing **a** conduction mode, **b** keyhole mode (partial penetration), and **c** keyhole mode (full penetration).

values of I_{corr} estimated using AEN (Table 1) and PPC (Table 2). Specifically, AEN analyses are associated with reduction reactions[62]. The low fractions of cathodic areas (IMCs and Fe) restricted oxygen access to these zones, resulting in a diffusion-controlled corrosion[61]. However, the partial penetration keyhole mode weld was an exception due to the mitigation of Fe cathode effects on the Al matrix (η-Fe_2Al_5 effect on IF steel) and the absence of a continuous IMC layer. This led to a mixed control mechanism and a dissimilarity in I_{corr} compared to the $I_{R.M.S.}$. These features were also responsible for its lowest I_{corr}. Subsequently, the full penetration keyhole mode weld demonstrated the next lowest I_{corr} due to the presence of a sufficient course η-Fe_2Al_5 and θ-Fe_4Al_{13} IMCs. I_{corr} of the conduction mode welding was comparable to that of the non-welded region because of the low penetration that does not permit Fe cathodic effect mitigation. It is important to note that I_{corr} was inversely proportional to R_4 (Table 2), validating the results due to their relation[63].

In the case of the interface between the weld and HAZ, the weld's higher potential acts as the cathode, while the HAZ area's lower potential acts as the anode. Pitting initiation on the Al-side HAZ originates from $FeAl_3$, an IMC formed through solid-state diffusion during the welding process. The pitting within the steel HAZ is primarily ascribed to changes in grain size, the presence of defects, dislocations, residual stresses[5], and η-Fe_2Al_5 cathodic effect[25]. The count of pits is greater within this area, and they are comparatively shallower when compared to those on the Al-side of the HAZ. This indicates the formation of the metastable pitting (activation-passivation cycling) on the steel-side HAZ. This was appreciated as the fluctuations over the time of the voltage (OCP) and current density (ZRA) (Fig. 3). The fluctuations on the PPC cathodic branch (Fig. 4) were also caused by these metastable pitting. Significant pitting was observed in the non-welded region of the Al sheet. These observations distinctly suggest the formation of a galvanic cell between the steel and Al sheets, with the Al experiencing anodic attack and the steel being shielded through cathodic polarisation[5]. The presence of this galvanic cell is further supported by the high chemical activity of the anodic branch (PPC, Fig. 4)[5].

In the ***non-welded region***, two corrosion mechanisms were observed: one at 2 hours and another at 24 hours or more of immersion (Fig. 10). The

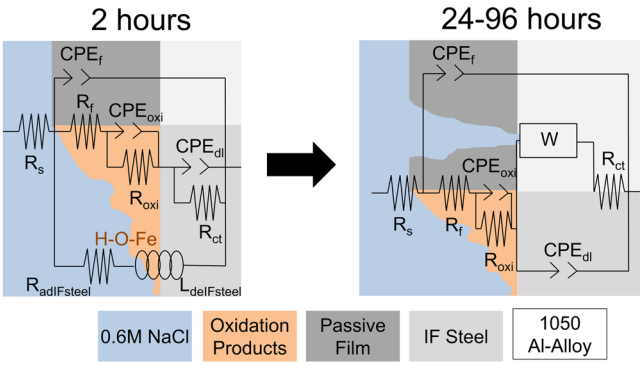

Fig. 10 | Evolution of corrosion mechanisms over time for non-weld area. Evolution over time of the non-welded 1050 Al alloy and IF steel region in 0.6 M NaCl: At 2 hours, the corrosion mechanism included the passive film of the Al, the Fe oxidised layer, the adsorption-desorption process, and exposed material. The adsorption-desorption process was replaced by the diffusion process after 24 hours.

2-hour mechanism involved processes such as passive film of the 1050 Al (second-time constant/ CPE_f, n_f, and R_f), oxidation products of the IF steel (third time constant/ CPE_{oxi}, n_{oxi}, and R_{oxi}), adsorption-desorption process of the steel (fifth time constant/ $R_{adIFsteel}$ and $L_{adIFstee}$), and bared materials (fourth time constant/CPE_{dl}, n_{dl}, and R_{ct}). The passive film is a typical element on Al (alloys)[64]. The SEM images revealed the presence of an oxidised layer on the steel (Fig. 8b). The electrochemical interaction between Al and steel influenced the formation and behaviour of the passive film, while the deposition of oxidation products from Al contributed to the oxidation processes occurring on the steel surface[34]. The adsorption-desorption process, stemming from the chemical reaction between hydroxide ions (OH-) and Fe, as shown in Eqs. (14) to (16), diminished in activity after 24 hours[20,39]:

$$Fe + H_2O \rightarrow FeOH_{ad} + e^- + H^+ \quad (14)$$

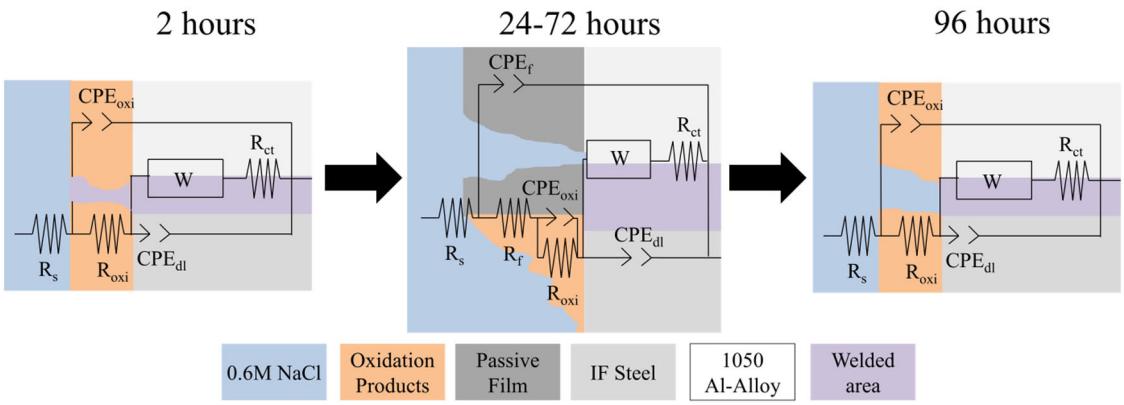

Fig. 11 | Evolution of corrosion mechanisms over time in the conduction mode weld. In 0.6 M NaCl: Initially, at 2 hours, the corrosion mechanism included the oxidised layer, the diffusion process, and exposed material. Between 24 and 72 hours, the passive film process was added to the corrosion mechanism. At 96 hours, the mechanism remained similar to that at 2 hours.

$$FeOH_{ad} \rightarrow FeOH^{+}_{ad} + e^{-} \quad (15)$$

$$FeOH^{+}_{ad} + H^{+} \rightarrow Fe^{+2} + H_2O \quad (16)$$

The adsorption-desorption process was replaced by a diffusion process. This process was observed to create cracks in the steels oxidised layer (Fig. 8b). Diffusion processes occurred due to pitting on the Al and the presence of cracks on the steels surface during longer immersion times[23], with the Fe's cathodic effect promoting the formation of pits[65]. The main disparity in the corrosion mechanisms at ≥ 24 hours was an increase in corrosion resistance, attributed to the accumulation and thickening of the oxidised product layer on the surfaces[34].

The corrosion system's complexity arises from the two materials' distinct chemical reactions with the environment. Al forms a compact passive film upon oxidation, while IF steel develops a heterogeneous oxidised layer prone to defects like porosity and cracks. This inherent dissimilarity in electrochemical behaviour between the Al passive film and the steel oxidised layer manifests in the EIS results. Notably, the adsorption-desorption process, driven by hydroxide-iron reactions, is exclusive to steel in neutral environments and absent in Al. Beyond individual material contributions, interactions such as galvanic corrosion and the generation of chemical products that react with other material further influence EIS outputs, reflecting the complex relationship of corrosion processes within the system.

The corrosion mechanism of the ***conduction mode*** weld during EIS testing evolved over time, revealing two distinct phases (Fig. 11). Initially, at 2 hours of immersion, the mechanism primarily involved the formation of oxidation products on both the Al passive film and IF steel surfaces, along with exposure of bare substrate material, and diffusion processes. The cathodic effect of IMCs within the weld, combined with the cathodic influence of the IF steel, significantly reduced the protective capacity of the Al passive film, leading to extensive pitting around the weld/Al interface (Fig. 8c)[52,65–69]. The reduced size of cathodic zones due to the welding process limited the ability of the oxygen and water for reduction reaction, thereby promoting diffusion processes. The welding process generates cathodic IMCs and modified electrochemical activities of IF steel. These phenomena lead to the reduction of the cathodic area. The absence of adsorption-desorption processes on the IF steel surface is likely due to microstructural and chemical changes caused by welding, which reduced the steel's affinity for hydroxide ions.

Between 24 and 72 hours, the corrosion mechanisms mirrored those observed in non-welded regions at the same immersion times. This is due to the corrosion and detachment of IMCs in saltwater, leading to a decrease in their cathodic effect on the Al matrix. This allowed for the formation of a passive film on the Al surface, although pitting was still observed in the Al-side HAZ due to the remaining cathodic influence of the IF steel[34,40].

At 96 hours, the corrosion mechanism resembled that of the initial 2-hour period, with the passive film compromised. The affinity of Al_2O_3 and $Al(OH)_3$ for Cl^- ions, coupled with the ongoing cathodic effect of the steel, contributed to the dissolution of the passive film and the exposure of new cathodic IMCs[22,70]. This led to further damage and impairment of the Al passive film.

The ***partial penetration keyhole mode weld*** exhibited a corrosion mechanism that evolved over time, characterised by two equivalent circuits (see Fig. 12). The initial corrosion mechanism observed within 24 hours of immersion, characterised by the formation of an Al passive film, an IF steel oxidised layer, IMC diffusion, and exposed bare substrate, resembled the mechanism found in the conduction mode weld between 24 and 72 hours. The lack of a continuous layer and the small size of IMCs promoted the formation of a passive film on the Al, reducing the material's chemical activity to form pitting at the Al/weld interface (Fig. 8d). The diffusion processes (first 2 hours of immersion) were affected by the discontinuous distribution and small size of IMCs, while at 24 hours, pitting also contributed to diffusion impedance[40]. This pitting was visible in the Al HAZ (Fig. 8d). By 48 hours of immersion, the corrosion mechanisms observed in the keyhole samples mirrored those found in the conduction mode weld at 96 hours, primarily consisting of an IF steel oxidised layer, diffusion processes, and exposed bare material. Similar to the conduction welded sample, the degradation of the Al passive film's protective capacity was driven by its affinity for chloride ions, the cathodic effect of the IF steel, and the exposure of new cathodic IMCs.

The corrosion mechanism evolution in the ***full penetration keyhole mode weld*** exhibited more changes compared to other samples, consisting of four corrosion mechanisms (Fig. 13). The initial corrosion mechanism (2 hours of immersion) included oxidation products of the IF steel, bared materials, Fe, and IMCs adsorption-desorption processes (sixth time constant/ R_{adIMC} and L_{IMC}). The higher welding penetration resulted in an increased number of Fe-bearing IMCs (without continuous layer) capable of undergoing adsorption-desorption processes. The intensity of corrosion process outputs in EIS directly correlates with the concentration and severity of these processes within the system. Process concentration is proportional to the areas where the process occurs. Therefore, the increase in the number and size of Fe-bearing IMCs made the IMC adsorption-desorption process visible in EIS measurements. The presence of IMCs hindered the formation of a protective passive film on the Al portion[65], and the increase in the size and concentration of the IMCs further exacerbated this hindrance. Over time (24 hours), the effectiveness of the adsorption-desorption process reduced due to IMC oxidation, reducing the cathodic effect of IMCs[34,40], thus

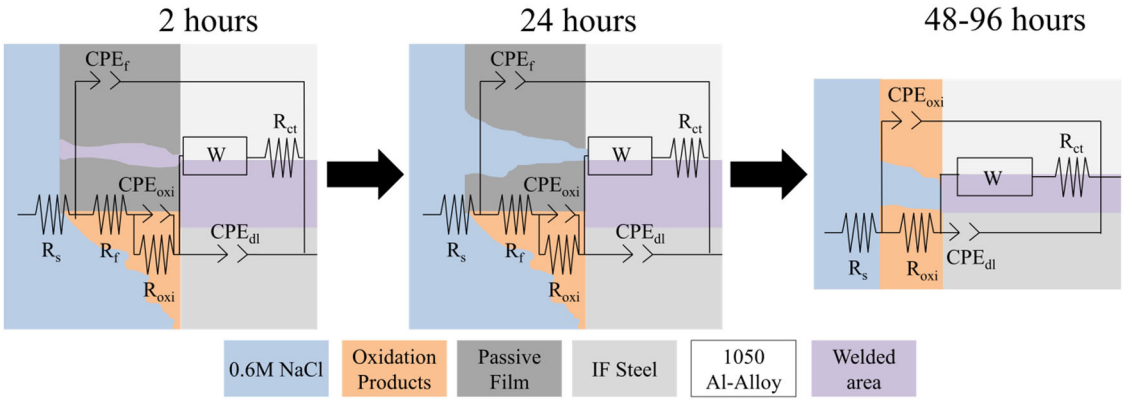

Fig. 12 | Evolution of corrosion mechanisms over time of the keyhole mode (partial penetration) weld. In 0.6 M NaCl: The corrosion mechanism for 24 hours or less comprised of the passive film, oxidised layer, diffusion process, and exposed material. The passive film was absent from the corrosion mechanism after 48 hours of immersion.

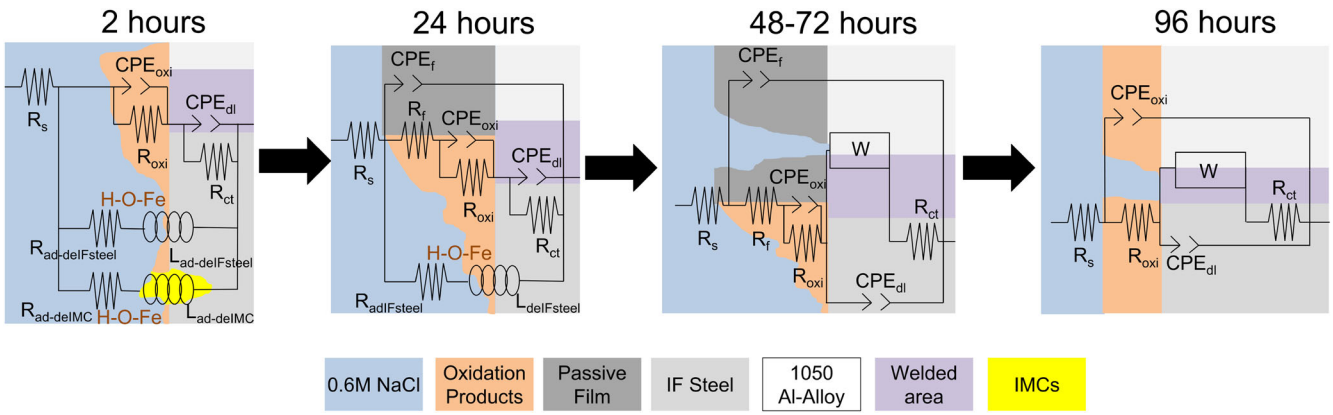

Fig. 13 | Evolution of corrosion mechanisms over time of the full penetration keyhole mode weld. In 0.6 M NaCl: The corrosion mechanism for 2 hours involved the oxidised layer, exposed material, intermetallic compounds (IMCs), and the Fe adsorption-desorption process. The IMCs adsorption-desorption process was replaced by the passive film process at 24 hours. The diffusion process then replaced the adsorption-desorption process in the corrosion mechanism at 48–72 hours. The passive film disappeared from the corrosion mechanism at 96 hours.

allowing the formation of the Al passive film and the elimination in EIS of the IMCs adsorption-desorption process. Therefore, the corrosion mechanism observed at 24 hours in the keyhole samples mirrored that of the non-welded region at 2 hours, primarily comprising an Al passive film, an IF steel oxidized layer, an iron adsorption-desorption process, and exposed bare material. Similar to the partial penetration keyhole mode weld, the corrosion mechanisms of this sample evolved through the generation of diffusion processes (pitting and crack formation) and the absence of the adsorption-desorption process (oxidation of Fe) during longer immersion periods (48–72 hours) (corrosion processes; Al passive film, IF steel oxidised layer, pitting and crack diffusion and, bare materials). At 96 hours, the corrosion mechanism mirrored that of the welded samples (IF steel oxidised layer, crack and pitting diffusion and, bared materials). The corrosion and detaching of the IMCs were observed in Fig. 8e as oxidised areas with cracks and pitting.

The differing evolution of corrosion mechanisms among the samples was influenced by both the welding penetration depth and the type and distribution of IMCs generated during welding.

In conclusion, this study highlights the varying corrosion behaviours observed across different interfaces of the dissimilar weld. The Al/weld interface exhibited significant susceptibility to GC due to the continuous layer of η-Fe_2Al_5 and θ-Fe_4Al_{13} IMCs, which acted as cathodic sites, leading to the dissolution of the surrounding Al matrix (anodic). Deep pitting was prominent in the Al-side heat-affected zone (HAZ), initiated by $FeAl_3$, while the steel-side HAZ displayed shallow pitting primarily due to microstructural changes. Additionally, defects such as cracks around the gap between the sheets and within the weld were also prone to corrosion. Within the weld, changes in composition and the formation of cathodic IMCs contributed to GC. The weld size and IMC distribution significantly influenced GC in dissimilar metal welding. Most samples exhibited corrosion controlled by diffusion in the cathodic branch and high activity in the anodic branch, with the partial penetration keyhole mode welding being the only exception, displaying mixed control for both branches. Corrosion mechanisms evolved over time due to changes in weld microstructure. However, after 96 hours, all welded samples showed similar corrosion mechanisms, with corrosion resistance improving over time due to the accumulation of oxidation products on the surface.

Methods

LBW was performed on the IF steel (Fe) (1 mm) to the 1050 aluminium (Al) alloy (3 mm), in an overlap configuration with the steel on top. In the current study, lean alloys were selected rather than multicomponent alloys, which allows a clear insight of the welding phenomena and IMC formation. This insight holds relevance for commercial alloys like mild steel (MS), Dual-phase (DP) steel, and 5xxx and 6xxx series wrought Al alloys employed in automotive applications. Coupons of 120 mm in length and 38 mm in width were used for the LBW process. Both materials did not have any coating (i.e., not galvanised) and were cleaned of any contaminations

using acetone prior to welding, chemical compositions of the materials can be found in Table 5. An adjustable ring-mode (ARM) laser was used for the process, which consisted of two 5000 W lasers (core and ring), Fig. 14 shows the setup for the LBW process. To achieve the different welding modes, three power combinations were used which are listed in Table 6. The welding speed, focal offset and ring power of the ARM laser were kept consistent between the 'three' weld types. More detailed studies about the effect of processing parameters on the weld microstructure can be found in previous research by the authors[11,15]. The lap shear test (load vs extension) results are presented in Fig. 15, according to the ISO 4136:2022 standard[71], conducted on an Instron 30 kN tensile testing machine.

Electrochemical analyses were conducted in the non-welded region and in the three welds (conduction, partially penetrated, and fully penetrated keyhole mode). Each test was repeated at least three times per sample to confirm the results. The analyses were performed using a potentio/galvanostat device (Interface1010E) and were managed through the Gamry framework software. The data analyses were performed with Gamry Echem analysis software. The testing was done using three electrode cells, being 3 M KCl silver/silver chloride (3 M Ag/AgCl) as reference electrode with double junction (EDT direct ion limited), a platinum wire with a diameter of 0.7 mm (Cooksonglod Heimerle + Meule Group) as the counter electrode while the samples were the working electrodes.

Table 5 | Chemical compositions (in wt. %) measured via optical emission spectroscopy (OES) and base material ultimate tensile strength (UTS) of the IF steel and 1050 Al alloy

IF steel	Fe	C	Mn	Al	Si	S	UTS (N/mm²)
	Bal.	0.05	0.165	0.05	0.03	0.01	210
1050 Al alloy	**Al**	**Si**	**Fe**	**Cu**	**Mg**	**Ti**	**UTS (N/mm²)**
	Bal.	0.08	0.47	0.006	0.001	0.025	110

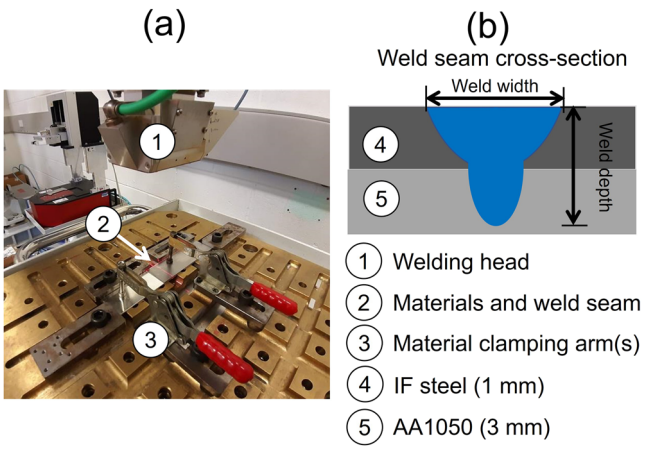

Fig. 14 | Welding photo and weld geometry. The setup for creating coupons using the **a** LBW set-up and **b** a schematic diagram showing a representative weld cross-section.

The laser-welded joints, and the non-welded plates were used as samples. It is important to note that the non-welded samples consisted of a 1050 Al-alloy and IF steel. To prepare for electrochemical testing, cross-sections were taken from the centre of the laser-welded samples. This ensured accurate results by avoiding irregularities often present at the beginning and end of a weld. The cross-sections were 5 mm thick and mounted in epoxy resin (VersoCit, Struer) to prevent crevice corrosion. After mounting, the samples (both welded and non-welded) were ground with P80 grit SiC paper to remove excess resin from the test and electrical contact areas. To achieve a smooth surface for testing, they were then polished with P400 and P1200 SiC paper, followed by 3 µm polycrystalline diamond paste. After the polishing process, the samples were kept for 48 hours to allow the formation of the native passive film on the sample. The samples were firstly cleaned with a commercial detergent and fresh water, then soaked with distilled water, lastly, they were sprayed with iso-propanol and subsequently dried. A well-defined exposed area was created on each sample using a punch to generate a hole in electrically insulating tape. To prevent crevice corrosion, the edges of the hole were then sealed with epoxy resin (Araldite). The exposed area on all samples was approximately 4 mm (height) × 2 mm (width), closely matching the dimensions of the weld zone (Fig. 16).

For each sample, the exposed area included a similar length of each metallic alloy, reflecting the thickness of the individual sheets (1 mm for IF steel and 3 mm for 1050 Al-alloy). This ensured consistency in the exposed areas of IF steel and Al across all samples. The immersion depth of the Pt counter electrode wire was set to the maximum length that wouldn't cause polarisation of the samples, thus maintaining their non-corroded potential.

The aggressive environment of the electrochemical assessments was a 0.6 M (35 g/mL) sodium chloride (supplied by Merck-Sigma-Aldrich) solution, naturally aerated, at room temperature. The volume of the aggressive environment was ≈ 60 mL. The electrochemical tests were non-perturbative (asymmetric electrochemical noise), perturbative with direct current (potentiodynamic polarisation curve), and alternating current (electrochemical impedance spectroscopy).

Asymmetric electrochemical noise (AEN) was formed of two non-perturbative electrochemical testing; open circuit potential (OCP) and zero resistance ammeter (ZRA) that were conducted at the same time. AEN was comprised of the reference, counter, and working electrodes[62]. OCP and ZRA were measured for 2 hours with a 0.05 s acquisition time. This technique was employed to evaluate the corrosion evolution at the short term and define the type of corrosion.

Potentiodynamic polarisation curves (PPC) were conducted with the following specific conditions. The initial potential was set at the potential at open circuit -0.3 V, and the voltage scan rate was 0.167 mVs^{-1}. The current density was limited to 1 $mAcm^{-2}$, and the final potential was defined at 2 V

Table 6 | Details of the LBW parameters used in this study

Parameter	Units	Welding mode		
		Conduction	Partial penetration keyhole	Full penetration keyhole
Ring laser power	W	5000 (Maximum)		
Core laser power		1000	1500	2500
Speed	m/min	4		
Wavelength	nm	1070 ± 10		
Focal offset	mm	16		
Focusing length	mm	300 mm (core and ring)		
Collimating length	mm	150	150	150
Spot diameter at focus	µm	200 (core) and 580 (ring)		

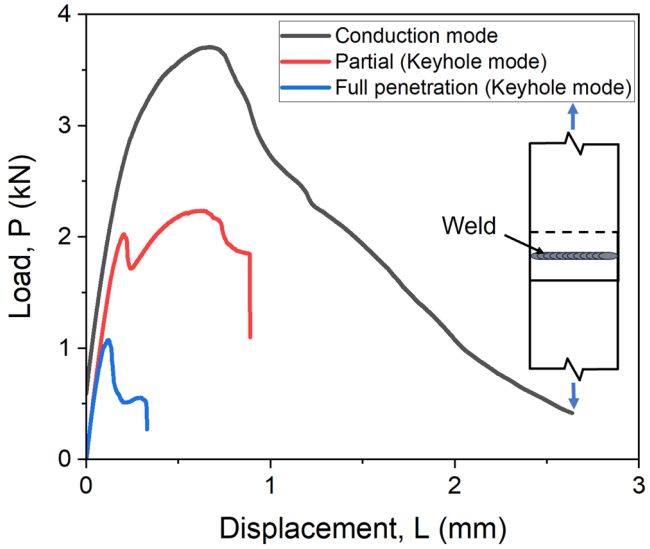

Fig. 15 | Load displacement curves. Data for conduction and keyhole (partial and full penetration) mode samples. The included image illustrates the geometry of the overlap configuration and the weld.

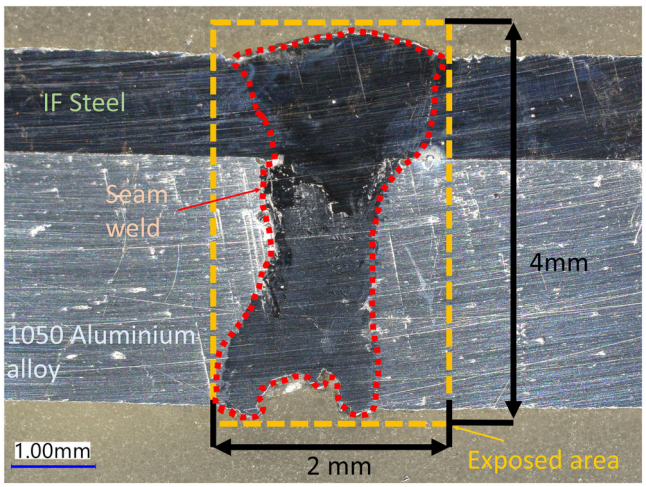

Fig. 16 | Electrochemical analysis region. Optical image of a weld cross-section, with the exposed area for electrochemical analysis testing, indicated.

versus the reference electrode potential. The potential at the open circuit was set after two hours of immersion in 0.6 M NaCl. The control reaction of the anodic and cathodic branch, corrosion current density, and potential were analysed with PPC.

Electrochemical impedance spectroscopy (EIS) was conducted at 10 mV root mean square (RMS) of potential amplitude with a frequency range from 10^{-2} Hz to 10^{5} Hz and 10 points per frequency decade. EIS tests were made at several immersion times in 0.6 M NaCl (at 2 hours, 24 hours, 48 hours, 72 hours, and 96 hours) to assess the corrosion mechanism evolution over the time of the samples. The equivalent circuit of the EIS data were obtained through Gamry Echem analysis software to evaluate the corrosion mechanism evolution over time.

Each type of electrochemical test was repeated a minimum of three times for each sample to ensure the reproducibility of the results.

The microstructure analysis of the welds was conducted both before and after the corrosion tests. For the corrosion test samples, they were carefully cut perpendicular to the weld and ground up to a P1200 SiC paper. Following the corrosion test, the samples were mounted in a conductive resin and further ground to eliminate any excessive corrosion products, thereby revealing the microstructural features. A Keyence VHX7000 light microscope was used for acquiring macro-scale images of the microstructure for the preliminary studies. For all high-resolution imaging and chemical mapping an FEI Versa scanning electron microscope (SEM) which was equipped with energy dispersive x-ray spectroscopy (EDS) was used. SEM micrographs were acquired using a secondary electron (SE) detector, for the purpose of distinguishing topographical microstructural features. An accelerating voltage of 20 kV and a current of 16 nA was used. For EDS chemical mapping a count rate of approximately 300,000 and pixel dwell time of 250 ms was used.

Data availability

Data will be made available on request.

Received: 23 May 2024; Accepted: 13 September 2024;
Published online: 11 October 2024

References

1. Kuryntsev, Sergey A review: laser welding of dissimilar materials. *Materials* **15**, 122 (2022).
2. Springer, H. et al. On the formation and growth of intermetallic phases during interdiffusion between low-carbon steel and aluminum alloys. *Acta Mater.* **59**, 1586–1600 (2011).
3. Matysik, P., Józwiak, S. & Czujko, T. Characterization of low-symmetry structures from phase equilibrium of Fe-Al system-microstructures and mechanical properties. *Materials* **8**, 914–931 (2015).
4. Li, Y., Liu, Y. & Yang, J. First principle calculations and mechanical properties of the intermetallic compounds in a laser welded steel/aluminum joint, *Opt. Laser Technol*. **122**, 10. https://doi.org/10.1016/j.optlastec.2019.105875 (2020).
5. Rahal, C. et al. Olive leaf extract as natural corrosion inhibitor for pure copper in 0.5 M NaCl solution: A study by voltammetry around OCP. *J. Electroanal. Chem.* **769**, 53–61 (2016).
6. Kotadia, H. R., Franciosa, P. & Ceglarek, D. Challenges and opportunities in remote laser welding of steel to aluminium, MATEC Web of Conferences, vol. 269, https://doi.org/10.1051/matecconf/201926902012 (2019).
7. Mohammadpour, M. et al. Effect of dual laser beam on dissimilar welding-brazing of aluminum to galvanized steel. *Opt. Laser Technol.* **98**, 214–228 (2018).
8. Sadeghian, A. & Iqbal, N. A review on dissimilar laser welding of steel-copper, steel-aluminum, aluminum-copper, and steel-nickel for electric vehicle battery manufacturing, *Opt. Laser Technol.* **146**, 10. https://doi.org/10.1016/j.optlastec.2021.107595 (2022).
9. Kimthong, P., Wattanapornphan, P., Waree, K., Uthaisangsuk, V. & Phongphisutthinan, C. Investigation of homogeneity of chemical and mechanical properties in laser-welded dissimilar steel-aluminum joints. *Chiang Mai J. Sci.* **48**, 1111–1128 (2021).
10. Cui, L., Chen, B., Qian, W. He, D. & Chen, L. Microstructures and mechanical properties of dissimilar Al/steel butt joints produced by autogenous laser keyhole welding, *Metals* **7**, https://doi.org/10.3390/met7110492 (2017).
11. Kotadia, H. R., Franciosa, P., Jabar, S. & Ceglarek, D. Remote laser welding of Zn coated IF steel and 1050 aluminium alloy: processing, microstructure and mechanical properties. *J. Mater. Res. Technol.* **19**, 449–465 (2022).
12. Xu, Y. et al., Correlation between the microstructure and corrosion behaviour of copper/316 L stainless-steel dissimilar-metal welded joints, *Corros. Sci.* **191**, 10. https://doi.org/10.1016/j.corsci.2021.109729 (2021).
13. Arenas, M. A., Bethencourt, M., Botana, F. J., De Damborenea, J. & Marcos, M. Inhibition of 5083 aluminium alloy and galvanised steel by lanthanide salts. *Corros. Sci.* **43**, 157–170 (2001).

14. Jabar, S. et al., Effect of a ring-shaped laser beam on the weldability of aluminum-to-hilumin for battery tab connectors, *J. Laser Appl*., **35**, 04, https://doi.org/10.2351/7.0001156 (2023).
15. Jabar, S., Barenji, A. B., Franciosa, P., Kotadia, H. R. & Ceglarek, D. Effects of the adjustable ring-mode laser on intermetallic formation and mechanical properties of steel to aluminium laser welded lap joints, *Mater. Des.* **227**, 11. https://doi.org/10.1016/j.matdes.2023.111774 (2023).
16. Ahuir-Torres, J. I., Gibbons, G. J., West, G., Das, A. & Kotadia, H. R. Understanding the corrosion behaviour of Al-Mg alloy fabricated using a Laser Powder Bed Fusion (L-PBF) Additive Manufacturing (AM) process. *J. Alloy. Compd.* **969**, 172300 (2023).
17. Öteyaka, M. Ö. & Ayrtüre, H. A study on the corrosion behavior in sea water of welds aluminum alloy by shielded metal arc welding, friction stir welding and gas tungsten arc welding. *Int J. Electrochem. Sci.* **10**, 8549–8557 (2015).
18. Amin, M. A. Metastable and stable pitting events on Al induced by chlorate and perchlorate anions-Polarization, XPS and SEM studies. *Electrochim. Acta* **54**, 1857–1863 (2009).
19. Wloka, J., Laukant, H., Glatzel, U. & Virtanen, S. Corrosion properties of laser beam joints of aluminium with zinc-coated steel. *Corros. Sci.* **49**, 4243–4258 (2007).
20. Basak, A. K., Diomidis, N., Celis, J. P., Masquelier, C. & Warichet, D. Chemical reactivity of thermo-hardenable steel weld joints investigated by electrochemical impedance spectroscopy. *Electrochim. Acta* **53**, 7575–7582 (2008).
21. Anaman, S. Y., Cho, H. H., Das, H., Lee, J. S. & Hong, S. T. Microstructure and mechanical/electrochemical properties of friction stir butt welded joint of dissimilar aluminum and steel alloys. *Mater. Charact.* **154**, 67–79 (2019).
22. Ahuir-Torres, J. I., Kotadia, H. R., Öpoz, T. T. & Sharp, M. C. A study on the corrosion behaviour of laser textured pure aluminium in saltwater, *Processes*, **11**, https://doi.org/10.3390/pr11030721 (2023).
23. Ma, Y. et al. Galvanic corrosion of AA5052/304SS welded joint with Zn-based filler metal in marine engineering. *Corros. Sci.* **211**, 110912 (2023).
24. Shi, Y., Li, J., Zhang, G., Huang, J. & Gu, Y. Corrosion behavior of aluminum-steel weld-brazing joint. *J. Mater. Eng. Perform.* **25**, 1916–1923 (2020).
25. De Graeve, I. et al. Mechanism of corrosion protection of hot-dip aluminium-silicon coatings on steel studied by electrochemical depth profiling. *Corros. Sci.* **76**, 325–336 (2013).
26. Lemmens, B. et al. Study of the electrochemical behaviour of aluminized steel. *Surf. Coat. Technol.* **260**, 34–38 (2014).
27. Sosa, E., Carbajal-De la Torre, G. & Espinosa-Medina, M. A. Assessment of the corrosion behavior of FeAl based intermetallics in NaCl solution. *ECS Trans.* **101**, 259–268 (2021).
28. Masmoudi, M., Mhadhbi, M., Escoda, L., Suñol, J. J. & Khitouni, M. Microstructural evolution and corrosion behavior of nanocrystalline FeAl synthesized by mechanical alloying. *J. Alloy. Compd.* **657**, 330–335 (2016). no. 2016.
29. Cottis, R. A. Interpretation of electrochemical noise data. *Corrosion* **57**, 265–285 (2001).
30. Kim, S. J. et al. Mechanical and electrochemical characteristics in sea water of 5052-O aluminum alloy for ship. *Trans. Nonferrous Met. Soc. China* **23**, 636–641 (2013).
31. Esmailzadeh, S., Aliofkhazraei, M. & Sarlak, H. Interpretation of cyclic potentiodynamic polarization test results for study of corrosion behavior of metals: a review. *Prot. Met. Phys. Chem. Surf.* **54**, 976–989 (2018).
32. Cavanaugh, M. K., Li, J.-C., Birbilis, N. & Buchheit, R. G. Electrochemical characterization of intermetallic phases common to aluminum alloys as a function of solution temperature. *J. Electrochem Soc.* **161**, 535–543 (2014).
33. Szklarska-Smialowska, Z. Pitting corrosion of aluminum. *Corros. Sci.* **41**, 1743-1767 (1999).
34. Ma, Y. et al. A novel corrosion transformation process in aluminum alloy/galvanized steel welded joint. *Corros. Sci.* **194**, 109936 (2022).
35. Org, W. E., Öteyaka, M. Ö. & Ayrtüre, H. ELECTROCHEMICAL SCIENCE A study on the corrosion behavior in sea water of welds aluminum alloy by shielded metal arc welding, friction stir welding and gas tungsten arc welding. Available: www.electrochemsci.org (2015).
36. ASTM G102-89 (2004)e1, Standard practice for calculation of corrosion rates and related information from electrochemical measurements, West Conshohocken, USA, 2004.
37. Smit, M. A., Hunter, J. A., Sharman, J. D. B., Scamans, G. M. & Sykes, J. M. Effects of thermal and mechanical treatments on a titanium-based conversion coating for aluminium alloys. *Corros. Sci.* **46**, 1713–1727 (2004).
38. MacDonald, D. D. Reflections on the history of electrochemical impedance spectroscopy. *Electrochim. Acta* **51**, 1376–1388 (2006).
39. Xu, Lning, Zhu, Jyang, xu Lu, M., Zhang, L. & Chang, W. Electrochemical impedance spectroscopy study on the corrosion of the weld zone of 3Cr steel welded joints in CO_2 environments. *Int. J. Miner.* **22**, 500–508 (2015).
40. Pan, Y. et al. Stress corrosion behavior of friction stir welding joint of 7N01 aluminum alloy. *J. Mater. Res. Technol.* **15**, 1130–1144 (2021).
41. Holm, S., Holm, T. & Martinsen, Ø. G. Simple circuit equivalents for the constant phase element. *PLoS One* **16**, 1–12 (2021).
42. Bisquert, J., Garcia-Belmonte, G., Bueno, P., Longo, E. & Bulhões, L. O. S. Impedance of constant phase element (CPE)-blocked diffusion in film electrodes. *J. Electroanal. Chem.* **452**, 229–234 (1998).
43. Wang, M., Qiao, C., Jiang, X., Hao, L. & Liu, X. Microstructure induced galvanic corrosion evolution of SAC305 solder alloys in simulated marine atmosphere. *J. Mater. Sci. Technol.* **51**, 40–53 (2020).
44. McCafferty, E. Introduction to corrosion science, Introduction to Corrosion Science, pp. 1–575, https://doi.org/10.1007/978-1-4419-0455-3 (2010).
45. Sabbaghzadeh, B., Parvizi, R., Davoodi, A. & Moayed, M. H. Corrosion evaluation of multi-pass welded nickel-aluminum bronze alloy in 3.5% sodium chloride solution: A restorative application of gas tungsten arc welding process. *Mater. Des.* **58**, 346–356 (2014).
46. Li, Y., Cai, J. M., Guan, L. & Wang, G. pH-dependent electrochemical behaviour of Al_3Mg_2 in NaCl solution. *Appl Surf. Sci.* **467–468**, 619–633 (2019).
47. Walter, G. W. A review of impedance plot methods used for corrosion performance analysis of painted metals. *Corros. Sci.* **26**, 681–703 (1986).
48. Orazem, M. E. & Tribollet, B. Electrochemical impedance spectroscopy. John Wiley and Sons. https://doi.org/10.1002/9780470381588 (2008).
49. Nisancioglu, K. Electrochemical behavior of Al3Fe intermetallic compound. *J. Jpn. Inst. Light Met.* **43**, 319–327 (1992).
50. Ezuber, H., El-Houd, A. & El-Shawesh, F. A study on the corrosion behavior of aluminum alloys in seawater. *Mater. Des.* **29**, 801–805 (2008).
51. Ambat, R., Davenport, A. J., Scamans, G. M. & Afseth, A. Effect of iron-containing intermetallic particles on the corrosion behaviour of aluminium. *Corros. Sci.* **48**, 3455–3471 (2006).
52. Hirata, K. et al. Size-dependent corrosion of Al-Fe intermetallic particles at Al-Mg Alloy surfaces investigated by in-liquid nanoscale potential measurement technique. *Small* **19**, 1–10 (2023).
53. Revie, R. W. Ed., Uhlig's Corrosion Handbook. John Wiley and Sons. https://doi.org/10.1002/9780470872864 (2011).
54. Zehra, S., Mobin, M. & Aslam, J. An overview of the corrosion chemistry. INC. https://doi.org/10.1016/B978-0-323-85405-4.00012-4 (2021).
55. Wu, H. et al. Effect of iron-containing intermetallic particles on film structure and corrosion resistance of anodized AA2099 alloy. *J. Electrochem Soc.* **165**, C573–C581 (2018).
56. Gecü, R. & Karaaslan, A. Volume fraction effect of stainless steel on microstructure, interface, corrosion and wear behavior of stainless

steel/aluminum bimetal composites. *Mater. Chem. Phys.* **284**, 126068 (2022).
57. Edeleanu, C. & Evans, U. R. The couses of the localized character of corrosion on aluminium. *Trans. Faraday Soc.*, **47**, 1121–1135 (1951).
58. Gnedenkov, A. S. et al. Corrosion of the welded aluminium alloy in 0.5 M NaCl solution. Part 1: Specificity of development, Materials, vol. 11, https://doi.org/10.3390/ma11102053 (2018).
59. Wang, X., li Chen, Y. & Niu, G. The study on corrosion resistance of high-strength spring steel. *Corros. Eng. Sci. Technol.* **53**, 54–64 (2018).
60. Goldstein, J. I. et al. Scanning electron microscopy and x-ray microanalysis. https://doi.org/10.1007/978-1-4939-6676-9 (2017).
61. Ahuir-Torres, J. I., Arenas, M. A., Perrie, W., Dearden, G. & de Damborenea, J. Surface texturing of aluminium alloy AA2024-T3 by picosecond laser: Effect on wettability and corrosion properties. *Surf. Coat. Technol.* **321**, 279–291 (2017).
62. Xia, D.-H. et al. "Review: Electrochemical Noise Applied in Corrosion Science: Theoretical and Mathematical Models towards Quantitative Analysis, *J. Electrochem. Soc.* **167**, https://doi.org/10.1149/1945-7111/ab8de3 (2020).
63. Kelly, R. G., Scully, J. R., Shoesmith, D. & Buchheit, R. G. Electrochemical techniques in corrosion science and engineering. https://doi.org/10.1201/9780203909133 (2002).
64. Bockris, J. O. M. & Minevski, L. V. On the mechanism of the passivity of aluminum and aluminum alloys. *J. Electroanal. Chem.* **349**, 375–414 (1993).
65. Thomä, M. et al. Ultrasound enhanced friction stir welding of aluminum and steel: Process and properties of EN AW 6061/DC04-Joints. *J. Mater. Sci. Technol.* **34**, 163–172 (2018).
66. Li, T., Wu, J. & Frankel, G. S. Localized corrosion: Passive film breakdown vs. Pit growth stability, Part VI: Pit dissolution kinetics of different alloys and a model for pitting and repassivation potentials, *Corros. Sci.* 182, **10**, https://doi.org/10.1016/j.corsci.2021.109277 (2021).
67. Grilli, R., Baker, M. A., Castle, J. E., Dunn, B. & Watts, J. F. Localized corrosion of a 2219 aluminium alloy exposed to a 3.5% NaCl solution. *Corros. Sci.* **52**, 2855–2866 (2010).
68. Dorin, T., Stanford, N., Birbilis, N. & Gupta, R. K. Influence of cooling rate on the microstructure and corrosion behavior of Al-Fe alloys. *Corros. Sci.* **100**, 396–403 (2015).
69. Ozdemir, F. et al. Corrosion behavior of a bulk nanocrystalline Al-Fe alloy, Corros Sci, vol. 209, no. 11, https://doi.org/10.1016/j.corsci.2022.110727 (2022).
70. Tighiouaret, S. et al. On the evolution of microstructure, texture and corrosion behavior of a hot-rolled and annealed AZ31 alloy, *Mater Chem Phys*. **267**, 12. https://doi.org/10.1016/j.matchemphys.2021.124598 (2021).
71. ISO 4136: 2022, Destructive tests on welds in metallic materials-Transverse tensile test. British standards (2022).

Acknowledgements

This work was partially supported by (1) LJMU pump prime funding, (2) WMG High Value Manufacturing Catapult Centre, (3) APC15 UK project ALIVE (Aluminium Intensive Vehicle Enclosures) grant number 50267 and (4) EPSRC MSI (Research Centre for Smart, Collaborative Industrial Robots) grant number EP/V062158/1. The authors would like to acknowledge the support provided by the WMG Characterisation Facility partially funded by Higher Education Funding Council for England (HEFCE) and the WMG High Value Manufacturing Catapult Centre.

Author contributions

Juan Ignacio Ahuir-Torres: Conceptualisation, data curation, visualisation, formal analysis, software, data curation, investigation, methodology, writing - original draft, writing – review & editing. Sharhid Jabar: Data curation, methodology, formal analysis, investigation, writing – original draft, writing – review & editing. Pasquale Franciosa: Software, validation, funding acquisition, supervision, resources, writing – review & editing. Darek Ceglarek: Funding acquisition, supervision, resources. Hiren R. Kotadia: Conceptualisation, visualisation, validation, resources, funding acquisition, formal analysis, supervision, writing – original draft, writing – review & editing.

Competing interests

The authors declare no competing interests.

Additional information

Correspondence and requests for materials should be addressed to S. Jabar or H. R. Kotadia.